2009-01-01

Characterizing The Deformation Of Reservoirs Using Interferometry, Gravity, And Seismic Analyses

Cara Schiek
University of Texas at El Paso, cgschiek@miners.utep.edu

CHARACTERIZING THE DEFORMATION OF RESERVOIRS USING

INTERFEROMETRY, GRAVITY, AND SEISMIC ANALYSES

CARA GINA SCHIEK

Department of Geological Sciences

APPROVED:

_____
José M. Hurtado Jr., Ph.D., Chair

_____
Aaron A. Velasco, Ph.D., Co-Chair

_____
Diane I. Doser, Ph.D.

_____
Bridget R. Konter, Ph.D.

_____
Sean M. Buckley, Ph.D.

_____
Patricia D. Witherspoon, Ph.D.
Dean of Graduate School

This part of my life is dedicated to Rich Schiek

Anne Grillet, and Jill Mizen. This would not have

been possible without your constant guidance, support,

and love. I will forever admire all of you in

every aspect of life.

CHARACTERIZING THE DEFORMATION OF RESERVOIRS USING INTERFEROMETRY, GRAVITY, AND SEISMIC ANALYSES

by

CARA GINA SCHIEK

DISSERTATION

Presented to the Faculty of the Graduate School of

The University of Texas at El Paso

in Partial Fulfillment

of the Requirements

for the Degree of

DOCTOR OF PHILOSOPHY

Department of Geological Sciences

THE UNIVERSITY OF TEXAS AT EL PASO

May 2009

ACKNOWLEDGEMENTS

All of work in this dissertation was funded by two NASA grants. The research conducted for the Deming, NM project was funded under NASA grant NNG04GR42G. The work in El Salvador was funded under the NASA Earth System Science Fellowship number NNX06AF78H. With this Fellowship, I was able to travel to Central America, and make great friends there, that I will never forget. I only hope that I can continue to do research with them.

I would first like to thank my committee members, Sean M. Buckley, Bridget Konter, Diane Doser, and Aaron Velasco; my collaborators, Galen Kaip, Demetrio Escobar, Vikas Gudipati, and Dochul Yang; and my family, Rich, Anne, and Jill. The combination of these people improved my thesis greatly. Sean, Vikas, and Dochul were great teachers, and provided me with a wealth of support in interferometry. Dochul, you are one in million, thank you for your very attentive help! Bridget, even though she came late in the game, was a huge help with learning how to forward model. I also feel it necessary to say that you are a truly inspirational young professor in every aspect, and specifically in your selflessness. Aaron, I seriously don't think I could have achieved this degree without your supportive ear. Thank you for being a great friend and mentor through the years. Galen, you will always be my favorite field partner! Rich, Anne, and Jill thank you for giving me the opportunity to achieve what you always believed I had in me.

I absolutely need to thank Tina Carrick, Carlos Montana, Pam Hart, and Sandy Ladewig. Thank you for helping me with the UTEP system. Carlos thank you for allows meeting my endless demands of computer space.

I would like to thank all the people I have worked with and taken classes from over my graduate experience. I would not be the scientist or person I am today without these experiences. I would especially like to thank Aaron Velasco, José Hurtado, Jr, Chris Andronicos, and Diane Doser. Your classes taught me how to be a geoscientist and how to use all of the tools available to me to answer my question. The graduate students that made the biggest impact on me would have to be Todd Theiner, Cleat Zeiler, Beverly House, Conor McDonough, Stephen Hernandez, and Yenlai Chee. Thank you guys for: your help; your wacky personalities that would always get me to laugh; and for being a true friend through it all. Stephen, thank you for all of your help and input. You have become a brother to me over the years, and if you ever need anything just let me know.

José thank you for teaching me how to be a researcher. You have been a great advisor. Your enthusiasm and optimism towards projects only helped me believe that there was an end in sight. Thank you for always 'coming along for the ride' as I would put it with my ideas about geological problems and projects that neither of us had any clue about in the beginning. If there were anyone in this experience that I have grown with, it would have to be you. We started at UTEP together, and have worked together for six years. You taught me how to be researcher in that time, and I have watched you become a great lecturer and advisor in that time.

During my time as a doctoral student, I fell in love with a wonderful man, Brian. You are my rock, my best friend, and the without a doubt the greatest part of my life. I anticipate our next great adventure in life! Hopefully this next one will not include breaking a car battery or getting a flat while off-roading in the desert.

ABSTRACT

In this dissertation, I characterize how reservoirs deform using surface and subsurface techniques. The surface technique I employ is radar interferometry, also known as InSAR (Interferometric Synthetic Aperture Radar). The subsurface analyses I explore include gravity modeling and seismic techniques consisting of determining earthquake locations from a small-temporary seismic network of six seismometers. These techniques were used in two different projects to determine how reservoirs deform in the subsurface and how this deformation relates to its remotely sensed surface deformation.

The first project uses InSAR to determine land subsidence in the Mimbres basin near Deming, NM. The land subsidence measurements are visually compared to gravity models in order to determine the influence of near surface faults on the subsidence and the physical properties of the aquifers in these basins. Elastic storage coefficients were calculated for the Mimbres basin to aid in determining the stress regime of the aquifers. In the Mimbres basin, I determine that it is experiencing elastic deformation at differing compaction rates. The west side of the Mimbres basin is deforming faster, 17 mm/yr, while the east side of the basin is compacting at a rate of 11 mm/yr. The second project focuses on San Miguel volcano, El Salvador. Here, I integrate InSAR with earthquake locations using surface deformation forward modeling to investigate the explosive volcanism in this region. This investigation determined the areas around the volcano that are undergoing deformation, and that could lead to volcanic hazards such as slope failure from a fractured volcano interior. I use the earthquake epicenters with field data to define the subsurface geometry of the deformation source, which I forward model to produce synthetic interferograms. Residuals between the synthetic and observed

interferograms demonstrate that the observed deformation is a direct result of the seismic activity along the San Miguel Fracture Zone. Based on the large number of earthquakes concentrated in this region and the fracturing suggested by the earthquake location results, I conclude that the southwestern slope of San Miguel is the most susceptible to volcanic hazards such as landsliding and flank lava flows.

Together these projects explore the dynamics of reservoir systems, both hydrologic and magmatic. They show the utility of geodetic remote sensing to constrain the relative importance of various, complex, subsurface processes, including faulting, fluid migration, and compaction.

TABLE OF CONTENTS

ACKNOWLEDGEMENTS……v

ABSTRACT……..vii

TABLE OF CONTENTS……..ix

LIST OF TABLES…….…...xii

LIST OF FIGURES……..……xiii

CHAPTER 1: INTRODUCTION……1

1.1 REFERENCES……..……..……..…….3

CHAPTER 2: DETERMINING THE INFLUENCES OF ANTHROPENGENIC LAND SUBSIDENCE IN THE MIMBRES BASIN NEAR DEMING, NM USING INSAR, GRAVITY, AND STORAGE COEFFICIENT CALCULATIONS……...4

ABSTRACT…….4

2.1 INTRODUCTION……..6

2.2 BACKGROUND…….....7

2.2.1 GEOLOGY…….....7

2.2.2 HYDROGEOLOGY & LAND SUBSIDENCE…….....7

2.2.3 INTERFEROMETRIC SYTHETIC APERATURE RADAR (INSAR)…….....8

2.2.4 AQUIFER STORAGE COEFFICIENT ESTIMATION…..……...……11

2.3 DATA PROCESSING.....12

2.3.1 INSAR DATA PROCESSING……..12

2.3.2 AQUIFER STORAGE COEFFICIENT ESTIMATION……..13

2.3.3 GRAVITY DATA ANALYSIS……14

2.4 RESULTS…..……15

2.4.1 INSAR RESULTS……16

2.4.2 AQUIFER STORAGE COEFFICENT ESTIMATE RESULTS……16

2.4.3 GRAVITY RESULTS……..19

2.5 DISCUSSION……..……..……...20

2.6 CONCLUSIONS..……..……...21

2.7 ACKNOWLEDGEMENTS……..22

2.8 REFERENCES……..23

CHAPTER 3: DETERMINING VOLCANIC DEFORMATION AT SAN MIGUELVOLCANO, EL SALVADOR BY INTEGRATING RADAR INTERFEROMETRY AND SEISMIC ANALYSES……..37

ABSTRACT…….37

3.1 INTRODUCTION…….39

3.2 BACKGROUND……..40

3.2.1 TECTONIC SETTING……..……..40

3.2.2 SAN MIGUEL VOLCANO…….……...41

3.2.3 INTERFEROMETRIC SYTHETIC APERATURE RADAR (INSAR)……..42

3.2.4 SEISMIC DEPLOYMENT……..…….44

3.3 DATA PROCESSING AND RESULTS.....45

3.3.1 INSAR DATA PROCESSING…….46

3.3.2 INSAR RESULTS…….47

3.3.3 SEISMIC PROCESSING……...……..48

3.3.3.1 *Automated Detection*……48

3.3.3.2 *Relative Earthquake Locations* ...……49

3.3.3.3 *Earthquake Location Classification*……...…….……50

3.3.3.4 *Local Magnitude*…..…..…..…..…..…..…...……...…….……51

3.3.4 SEISMIC PROCESSING RESULTS…....…….…..52

3.4 DISCUSSION…...……...……..52

3.5 CONCLUSIONS……..58

3.6 ACKNOWLEDGEMENTS……...60

3.7 REFERENCES…….61

CHAPTER 4: SYNTHESIS…….…….…….....85

4.1 REFERENCES……..……..……..……88

APPENDIX A: TUTORIAL FOR SEISMIC PROCESSING.....89

APPENDIX B: INPUT FILES FOR HYPODD.....92

CURRICULUM VITAE……96

LIST OF TABLES

Table 2.1: Interferograms used in SVD velocity displacement analysis. SAR images were acquired from a descending orbit……...……28

Table 2.2: Elastic storage coefficients calculated from ratio of subsidence rate to groundwater level decline rate.……...……28

Table 3.1: Image pairs used in InSAR analysis……...……..66

Table 3.2: Earthquake locations with calculated M_L..……...…….67

Table 3.3: List of parameters used in surface deformation forward model...……..…..…70

Table 3.4: Root Mean Square (RMS) error between interferogram and corresponding model…71

LIST OF FIGURES

Figure 2.1: Map of the Deming, NM. Inset shows study area location. Blue line is the Florida Mountain Fault. Fault traces were obtained from the USGS Quaternary Fault and Fold Database of the United States (http://earthquake.usgs.gov/regional/qfaults/). Squares are groundwater well locations. Dots are earth fissures. Green dot is earth fissure shown in Figure 2.3a. Red dot is earth fissure shown in Figure 2.3b. Black line is approximate location of gravity and InSAR profiles……...29

Figure 2.2: Water level decline from 1910 to 1990. Black dots indicate earth fissure locations. Contours are in meters. From Contaldo and Mueller (1991)……..……..……30

Figure 2.3: (a) Google Earth image depicting earth fissure (black line) curvilinear geometry. (b) Google Earth image showing orthogonal-polygonal earth fissure geometry..…….…....30

Figure 2.4: Flattened interferograms of the Mimbres Basin: (a) 04/23/93 – 09/10/93, (b) 11/13/95 – 01/06/97, (c) 01/06/97 – 11/17/97. White line indicates the trace of the surface subsidence profile shown in Figure 2.8. Black dashed ellipse is the approximate outline of the observed subsidence feature. One full color fringe is equal to 2.8 cm of subsidence in the LOS of the radar satellite……...31

Figure 2.5: Comparison of USGS wells groundwater level (diamonds) and InSAR-derived LOS surface displacements (squares) changes at five well locations shown in Figure 2.1. Errors for subsidence values are shown at individual points. Slopes of the trend lines are given in Table 2.2..……...……..…….…...32

Figure 2.6: (a) Bouguer gravity anomaly map. Data obtained from the Pan-American Center for Earth and Environmental Sciences (http://paces.geo.utep.edu/gdrp). Dots are data point locations used to create the Bouguer anomaly grid. (b) Second vertical derivative or high pass filtered (in eotvos) calculated from the Bouguer gravity anomaly map in (a). The white line represents the profile used for gravity models shown in Figure 2.7 and 2.8. One eotvos equals $1x10^{-6}$ mGals/cm……...……...…….33

Figure 2.7: (a) Gravity profile from white line in Figure 2.6b. Points are the observed measured gravity. Black line is the gravity calculated from the model shown in (b). Red line is the error (observed gravity – calculated gravity). (b) Two-dimensional gravity model for a profile (white line in Figure 2.6b) through the Mimbres Basin. Model parameters are based on work by Heywood (2002) and Mack et al., (1997). FMF = Florida Mountain Fault. A indicates location of Basin's maximum thickness..……..……..…….....……..34

Figure 2.8: Comparison of gravity profile (top) from Figure 2.7a and InSAR-derived LOS surface displacement (middle) and velocity (bottom) profiles from Figure 2.4(a-c) derived the SVD velocity displacement technique. A is the basin maximum thickness. FMF corresponds to the location of the Florida Mountain Fault……...…….……35

Figure 2.9: 11/13/95 – 03/17/97 interferogram with Earth fissure locations (black circles) and well locations (squares). Inset indicates areas of different subsidence rates. Oval on interferogram refer to area on inset. Same color scale is used as in Figure 2.4……...……...…….……...36

Figure 3.1: Map of San Miguel volcano (Escobar, 2007). Inset shows location of study area in El Salvador. Black dashed line in inset indicates location of El Salvador Fault Zone (ESFZ). Gray shaded area around black dashed line is the Median Trough. Green lines are fractures mapped by SNET. The fracture marked A is the San Miguel Fracture Zone (SMFZ). Triangles denote seismometers. Circles are locations of the vents that fed historic lava flows within the year of eruption. Squares are small villages. Black polygon in upper right is the city of San Miguel. Red lines are highways. Red and yellow arrows represent the tensile stress direction for the SMFZ.……....……...……....72

Figure 3.2: Historic seismicity (1984 – 2007) map (Escobar, 2007). Triangles denote the locations of seismometers in the temporary seismic network. Historic seismicity has been recorded by SNET seismometers at PAC, LAC, VSM, and BM. The historic seismicity has a local magnitude (M_L) range of 1.5 – 5. Green through brown contours indicates elevation. Cross is San Miguel volcano summit..……...……...……...……73

Figure 3.3: Interferograms of San Miguel volcano: (a) 02/27/07-10/15/07, (b) 03/03/07-10/19/07, (c) 10/15/07-01/15/08, and (d) 10/19/07-01/19/08. Interferograms (a) and (c) are obtained from ascending orbits. Interferograms (b) and (d) are obtained from descending orbits. Interferograms, (a) and (c), prior to mid-October 2007 show inflation. The interferograms, (b) and (d), after mid-October 2007 show deflation, and have negative motion (e.g. away from the satellite). White lines indicate profiles in Figure 3.4. Gray areas are decorrelated regions in the interferogram.……...……...……...……...74

Figure 3.4: Deformation profiles from the interferograms in Figures 3.3. Positive red profiles show inflation, and are taken from Figures 3.3(a-b). Negative red profiles show deflation, and are taken from Figures 3.3(c-d). Black, green, and purple are forward model profiles..……...……...……...75

Figure 3.5: Hypocenter sensitivity test. Each cross-section is 9 km wide and 6 km deep. Sections are taken along profile line D-D' in Figure 3.8. Columns are model runs with same constraint and weight. Rows are model runs with same seed depth. Black circles are calculated locations using the given parameters. Green squares are historic seismicity from SNET (1986-2007) (Escobar, 2007). Red star denotes the preferred locations and cross-section used in the surface deformation forward model..……...……...……...…76

Figure 3.6: Epicentral locations from the temporary seismic deployment (March 2007 – January 2008) with historic activity (1984 – 2007) (Escobar, 2007).…….....…….……..78

Figure 3.7: Example seismic events with different source types from our classification: (a) Tectonic; (b) Tectonic with Volcanic Tremor; (c) Tectonic with a Precursory Event and Volcanic

Tremor; (d) Volcanic Tremor. Top panel of each set is the calculated spectrogram. Each spectrogram depicts the frequencies captured at a specific time in the waveform. Bottom panel of each set is the seismogram used to calculate the spectrogram. Seismograms are from the VSM station……..……..……79

Figure 3.8: Hypocentral locations of events with different source types. (a) Classified earthquake locations using the results of the temporary seismic network and SNET (Escobar, 2007) historic data. (b) Cross-section at northern end. (c) Cross-section at southern end. (d) Cross-section along strike of the SMFZ. Cross-sections (b) and (c) include events 2 km from the profile line..……...…….……..……..81

Figure 3.9: Epicentral earthquake locations listed in Table 3.2 scaled to local magnitude (M_L). These magnitudes represent classified earthquakes of types 1-3..…….……82

Figure 3.10: Results from Yang forward model. LOS displacement map (left column) with corresponding synthetic LOS interferograms (middle column), and residual map (right column). Yang source parameter models are based on seismic analysis results and work by Chesner et al. (2004). White circle is the outline of summit crater at San Miguel. Black line indicates profile shown in Figure 3.4. Color scale given at the end of row corresponds to that row. Black dashed line is the placement of the SMFZ. Models include noise addition from corresponding interferogram correlation map.....…….....……..83

Figure 3.11: Temporal distribution of the classified earthquakes (not including historic events) shown in Figure 3.8. Numbers in bars are average M_L results for that event type during that month. Line represents average rainfall of El Salvador from BBC (2008)..…….84

CHAPTER 1

INTRODUCTION

Over the past decade, integrating Interferometric Synthetic Aperture Radar (InSAR), geophysical data, and geologic interpretations has become an increasingly important method for studying the surface to subsurface interaction of reservoir systems. InSAR has the ability to resolve many types of near-vertical surface deformation with both high resolution and high accuracy (Bürgmann et al., 2000). The large amount of available data for InSAR analysis enables time-series processing to be done for geologic monitoring. These time-series results can be integrated with subsurface geophysical data, such as earthquake locations, and 2-D gravity or magnetic modeling (e.g., William-Jones and Rymer, 2000; Schiek et al., 2006; Schiek et al., 2008; Buckley et al., *in review*). The integration of surface and subsurface data can be done using forward and inverse modeling techniques. The result of this integration leads to time-series observations and monitoring of how geologic systems respond to changing environmental parameters.

The goal of this dissertation is to characterize surface and subsurface deformation patterns in reservoir systems. The interaction between the surface deformation patterns and geophysically derived subsurface structures is explored through modeling, and enables an understanding of how these complex, dynamic systems work. This goal is approached in two projects with following common objectives:

- To utilize InSAR for detecting and quantifying surface deformation;
- To integrate surface deformation data with geophysical measurements to build structural and deformational models of a reservoir;

- To determine the relationships between measured surface deformation fields and subsurface structures.

The work completed in this dissertation ultimately yield insights into how surface deformation is related to subsurface processes.

The two projects are each discussed in their own chapter. The first project considers an area undergoing aquifer depletion resulting in land subsidence near Deming, NM. Chapter 2, "Determining the Influences of Anthropogenic Land Subsidence in the Mimbres Basin Near Deming, NM using InSAR, Gravity, and Storage Coefficient Calculations", will be submitted to *Geosphere*. This project combines gravity modeling with aquifer storage coefficients calculated from InSAR and groundwater level observations to determine how an aquifer and its accompanying geologic material deform.

The second project models of volcanic inflation and deflation caused by subsurface magmatic processes. This project focuses on San Miguel volcano, El Salvador. InSAR analyses of San Miguel volcano are used to determine the spatial extent and types of deformation occurring at the volcano. Earthquake locations calculated from a nine-month seismic deployment are used to build a forward model of surface deformation and compare to the interferometry results. This work, "Determining Volcanic Deformation at San Miguel Volcano, El Salvador by Integrating Radar Interferometry and Seismic Analyses", is described in Chapter 3. It will ultimately be split into two manuscripts, one for submission to the *Journal of Volcanology and Geothermal Research* and the other to the *Seismological Research Letters*. The *Journal of Volcanology and Geothermal Research* manuscript will describe the InSAR and forward modeling aspects of the project. The manuscript for the *Seismological Research Letters* will describe the seismology part of the project.

1.1 REFERENCES

Buckley, S.M., Gudipati, K., Schiek, C.G., Leuro, E., and Hurtado, J.M. (Jr.), in review (*Journal of Hydrology*), Ground deformation measurements and Hueco Bolson aquifer properties near El Paso, Texas from radar interferometry and gravity.

Buckley, S.M., 2000. Radar Interferometry Measurement of Land Subsidence, Ph.D. Thesis, University of Texas at Austin.

Bürgmann, R., Rosen, P.A., and Fielding, E.J., 2000, Synthetic aperture radar interferometry to measure Earth's surface topography and its deformation: *Annual Reviews of Earth and Planetary Science*, v. 28, p. 169-209.

Schiek, C.G., Luero, E, Buckley, S., and Hurtado, J., 2006, Characterization of anthropogenic land subsidence, its relation to fault system geometry, and their consequences for water table position in the El Paso, Texas area, using InSAR and gravity. *Eos Transactions American Geophysical Union,* vol. 87, no. 52, Fall Meeting Supplement, Abstract G43B-0999.

Schiek, C.G., Theiner, T., Velasco, A. A., and Hurtado, J.M. (Jr.), 2008, Preliminary volcanic modeling at San Miguel volcano, El Salvador using InSAR and seismic techniques. *Seismological Research Letters*, v.79 no.2, p.320.

Willian-Jones, G., and Rymer, H., 2000, Detecting volcanic eruption precursors: A new method using gravity and deformation measurements: *Journal of Volcanology and Geothermal Research*, v. 113, p. 379-389.

CHAPTER 2:

DETERMINING THE INFLUENCES OF ANTHROPENGENIC LAND SUBSIDENCE IN THE MIMBRES BASIN NEAR DEMING, NM USING INSAR, GRAVITY, AND STORAGE COEFFICIENT CALCULATIONS

ABSTRACT

Interferometric Synthetic Aperture Radar (InSAR) is used to observe land subsidence in the Mimbres Basin, southwestern NM during the 1990s. The subsidence is a consequence of aquifer depletion from area's lack of groundwater recharge in its arid climate and the ground water pumping required to meet the agricultural and municipal demands of Deming, NM. InSAR observations show a maximum of 9.2 cm of subsidence from 1992 to 1997. The interferometry results and recorded groundwater level changes are used to calculate multi-year storage coefficients for the Mimbres Basin aquifer at five local wells. The coefficients range from 3.5 x 10^{-3} to 16 x 10^{-3}. Spatially, the results define two distinct areas. The first, comprising most of the basin, defines an area where the basin sediments are undergoing compaction rates of 11 mm/yr. The second is a ~12 x 9 km area located in the western-central part of the basin. This second area is deforming at a faster rate, 17 mm/yr, and is outlined by earth fissures. This second region is the part of the basin undergoing the greatest amount of water-level decline and ground surface subsidence. A 2-D gravity model was constructed in order to determine the subsurface structures located in the vicinity of the subsidence bowl and different deformation zones. A geographic comparison of the gravity model with the two deformational zones shows that the ~15 mm/yr subsidence area coincides with the deepest part of the basin. This amount of subsidence could be the result of compaction within a thick deposit of lacustrine clays occurring in the deepest part of the basin or subterranean cavity filling.

KEYWORDS: Radar Interferometry; SVD displacement velocity method; Mimbres Basin; Gravity; Storage coefficients; Land subsidence; Earth fissures

2.1 INTRODUCTION

Anthropogenic land subsidence in the Mimbres Basin, concentrated around Deming, NM (Figure 2.1), is observed from Interferometric Synthetic Aperture Radar (InSAR) analyses spanning 1992 to 2000. This land subsidence is a consequence of aquifer depletion resulting from evapotranspiration and increasing amounts of water pumping required to meet the growing agricultural and municipal demands of Deming, NM since the 1910s.

InSAR, gravity measurements, and groundwater level are integrated to achieve these goals:

1. Measure spatial extent and magnitude of land subsidence in Deming, NM from 1992-1997;
2. Determine any relationships between the InSAR-observed subsidence pattern in the Mimbres Basin with subsurface structures derived from 2-D gravity modeling; and
3. Determine the compaction elasticity at five well locations in the Deming, NM area using a multi-year cumulative InSAR-derived deformation estimation technique.

An InSAR displacement velocity method is used to answer objective 1. Profiles taken from the InSAR analysis are compared to a 2-D gravity profile to solve objective 2. Cumulative multi-year InSAR measurements are combined with groundwater level data at five wells to calculate storage coefficients to meet objective 3. This calculation aids in establishing regions of elastic and inelastic compaction deformation.

2.2 BACKGROUND

2.2.1 GEOLOGY

The Mimbres Basin lies at the transition from the Rio Grade rift to the Basin and Range province (Heywood, 2002). The Mimbres Basin has a half-graben structure (Mack et al., 1997) created by the Florida Mountain Fault (FMF) (Figure 2.1), a normal fault that forms the eastern boundary of the basin (Hanberg and Frisen, 1995; Mack et al., 1997; Heywood, 2002). The FMF also creates the deepest part of the basin, which is the ~1 – 2 km (Heywood, 2002).

The basin sediments consist of two groups, the upper and lower sedimentary packages (Contaldo and Mueller, 1991). The upper sedimentary unit is composed of unconsolidated fluvial sediments consisting of gravel, sand, silt, and clay. This unit represents late Quaternary fan-delta sediment from the Mimbres River and is approximately 150 m thick (Contaldo and Mueller, 1991). The lower sedimentary unit is finer-grained than the upper unit and primarily consists of reddish clays (Contaldo and Mueller, 1991). This layer represents middle Pleistocene or older alluvial fan and lacustrine deposits and spans a depth of ~150 m to the top of bedrock at 1-2 km (Contaldo and Mueller, 1991). Bedrock consists of Cenozoic basaltic and andestic rocks, Paleozoic limestones and dolestones, and Precambrian plutonic rocks (Heywood, 2002).

2.2.2 HYDROGEOLOGY & LAND SUBSIDENCE

The main aquifer in the Mimbres Basin is contained within the unconsolidated sediments of the upper sedimentary unit (Contaldo and Mueller, 1991). This aquifer is mostly unconfined throughout the basin, although areas where the aquifer is confined have been described by Darton (1915, 1916) and Theis (1938). The transmissivity of the aquifer varies from 173.9 to 2358.2 m^2 per day (Contaldo and Mueller, 1991). The specific capacity of the wells in the

aquifer varies from 9.6 x 10^{-3} to 2.0 s^{-1} per meter of drawdown (McLean, 1977). The large range in the transmissivity and specific capacity values are due to alternating clay and sand beds throughout the basin (Contaldo and Mueller, 1991).

This Mimbres Basin aquifer has been the main source of water for the city of Deming, NM since the early 1910s (Contaldo and Mueller, 1991). In 1985, total groundwater withdrawal and depletion from storage was 131.7 x 10^6 m^3 (Wilson, 1985), and the groundwater level has declined ~35 m at a rate of ~0.44 m/yr between the 1910s and the 1990s (Contaldo and Mueller, 1991). This amount of groundwater depletion, and the lack of recharge from the less than 0.75 m/yr of desert monsoonal rains (Heywood, 2002) has created a large groundwater cone of depression in the Mimbres Basin, with the maximum amplitude of ~36 cm over 40 years (Figure 2.2) (Contaldo and Mueller, 1991). This cone of depression has an elliptical shape with the long axis pointing NNE (Contaldo and Mueller, 1991). Circling the edges of the cone of depression are at least eleven earth fissures that indicate surface deformation (Figure 2.2). These are large, mode 2 (Haneberg and Friesen, 1995) surface cracks, the youngest of which have appeared since ~1980 and have a curvilinear geometry (Figure 2.3a). Older fissures from the mid-1950s have an orthogonal-polygonal geometry (Figure 2.3b). The different morphology and topology of the older fissures may result from multiple fissures growing together over time (Contaldo and Mueller, 1991).

2.2.3 INTERFEROMETRIC SYTHETIC APERATURE RADAR (INSAR)

InSAR is a powerful tool for measuring surface deformation associated with groundwater pumping and aquifer compaction. Recent studies that use interferometry for monitoring and detecting anthropogenic land subsidence are Galloway et al. (1998) (Mojave Desert, California),

Amelung et al. (1999) (Las Vegas, Nevada); Buckley (2000) (Phoenix, Arizona), Valentine et al. (2001) (San Luis Obispo County, California), Heywood et al. (2002) (Albuquerque, NM), Cabral-Cano et al. (2008) (Mexico City, Mexico), Anderssohn et al. (2008) (Kashmar Valley, northeast Iran), Kim et al. (2008) (Mokpo City, Korea), and Buckley et al. (*in review*) (El Paso, Texas).

InSAR uses synthetic aperture radar (SAR) data to measure near-vertical (in the range direction, or line-of-sight, from the antenna) surface displacements (e.g Massonnet and Feigl, 1998). To do this, the difference in phase between two time-separated SAR images is determined. This phase difference is a combination of five effects: (1) differences in the orbital parameters between the two input images; (2) systematic and environmental noise; (3) atmospheric noise; (4) topography; and (5) ground deformation (Lu et al., 2007). In order to obtain an interferogram that primarily shows ground deformation, a two-step process is used. The first step is to select image pairs for the analysis. The first criterion for selecting images is to use image pairs with small differences in their satellite orbit parameters, or baselines (Massonnet and Feigl, 1998). This criterion minimizes the orbital and systematic noise effects (Lu et al., 2007). A second criterion is to use images containing little or no vegetation. This will reduce environmental noise that, for example, arises from changing vegetation patterns, and that often results in temporal decorrelation between image pairs, making interferograms difficult or impossible to compute.

The second step in isolating the deformation signal is to remove the influence of topography in the interferogram (Price and Sandwell, 1998; Bürgmann et al., 2000). Topography is removed by first using an accurate digital elevation model (DEM) and the imaging geometry of the input SAR images to generate a synthetic interferogram (Massonnet

and Feigl, 1998; Bürgmann et al., 2000). This synthetic interferogram is subtracted from the raw interferogram obtained from the input SAR images, resulting in a ground deformation interferogram. For this project, ERS-1/2 SAR data is used in Gamma Remote Sensing Software. These data were acquired during a time span from 1992 to 1997.

Temporal changes in atmospheric conditions and surface scattering are among the most important limitations to the application of InSAR. At the ERS-1/2 radar frequency, 5.3 GHz (C band), changes in land use, including urbanization and agriculture activities, can lead to decorrelation. Fortunately, Deming lies in a desert environment with relatively sparse vegetation, and some of these effects are minimized, allowing the generation of interferograms to detect centimeter scale ground subsidence over several years.

Once ground deformation interferograms are made, a subset of interferograms are chosen to use in a Singular Value Decomposition (SVD) displacement velocity technique developed by colleagues Krishnavikas Gudipati and Dochul Yang, based on the Small Baseline Subset (SBAS) InSAR algorithm (Berardino et al., 2002). This method is used to connect different temporal subsets of data. The group of interferograms chosen for this analysis is given in Table 2.1. These interferograms were chosen for their amount of coherent data located in the basin, overlapping time spans, and low atmospheric artifacts. The SVD displacement velocity method is preferred over the SVD displacement methods due to its use of overlapping velocity interferograms instead of interconnected displacement interferograms. The use of overlapping interferograms and the transformation from displacement to velocity is done in order to retain phase coherence over periods of missing data in the temporal span of the time-series (Berardino et al., 2002).

2.2.4 AQUIFER STORAGE COEFFICIENT ESTIMATION

A storage coefficient, also known as the specific storage, is the volume of water expelled or stored per unit area of aquifer for a unit change in water level (Fetter, 2001). Co-author, Krishnavikas Gudipati, in Buckley et al. (*in review*), estimates aquifer storage coefficients for the Hueco Basin in El Paso, TX in order to determine whether compaction in the basin is elastic or inelastic. If the resulting storage coefficient is elastic, then the observed compaction is recoverable. However if the storage coefficient is inelastic then the compaction is not recoverable and the sediments have lost pore space. To determine if a storage coefficient is elastic or inelastic, the hydrologic properties of the basin, such as preconsolidation and effective stress values, need to be constrained. If these parameters are unknown, then the basin can instead be compared to another basin with known hydrologic properties and similar hydrologic environment.

I use the same technique in this study to determine the state of compaction in the Mimbres Basin. The analysis in Buckley et al. (*in review*) is modeled after a study done by Hoffman et al. (2001) in which elastic storage coefficients are estimated from seasonal fluctuations in groundwater levels and in ground displacement measured with InSAR. Buckley et al. (*in review*) does this a multi-year scale using SVD interferometry and ground water level heights. This procedure has the following assumptions: (1) effective stress changes are the result of changes in pore fluid pressure; and (2) changes in pore-fluid pressure can be inferred from changes in water level due to variations in hydraulic head. The data utilized for this technique are subsidence measurements from multi-year interferometry and groundwater level data from five wells in the Mimbres Basin (Figure 2.1; wells 3-7). Wells 1 and 2 were excluded from the analysis due to insufficient ground water data. The well data is from the United States

Geological Survey (USGS) National Water Information System (http://waterdata.usgs.gov/nwis). The groundwater level data was collected at each well in the basin every five years beginning in 1958.

2.3 DATA PROCESSING

This section describes the data processing techniques used in this study. First, a radar interferometry analysis was used to determine the magnitude of subsidence, its spatial pattern, and the extent of the subsidence bowl (Schiek et al., 2006). These results were used with groundwater level data to calculate the elastic storage coefficient at each well site. A separate gravity analysis was done to determine the relationship between subsurface structures and the known surface deformation.

2.3.1 INSAR DATA PROCESSING

A two-pass InSAR technique (Massonnet and Feigl, 1998) was first applied to forty ERS-1/2 radar images of Deming spanning from 1992 to 2002 using the Gamma Remote Sensing Interferometry package. A total of 29 two-pass interferograms were made. Topography was removed from the interferograms using a 30-m resolution Shuttle Radar Topography Mission (SRTM) DEM. The results from this analysis are shown in Figure 2.4. These results display a subsidence feature west of the Florida Mountains (Figure 2.4). Apparent in many of the interferograms are topographically-induced atmospheric phase variations over the Florida Mountains, located to the east of the subsidence bowl, and at the bottom corners of the interferograms. This noise can be attributed to differences in the amounts of water vapor in the atmosphere between the two radar image acquisition dates (Figure 2.4). Unfortunately

interferograms produced using scenes acquired before 1995 have a high amount of atmospheric effects (Figure 2.4a). Fortunately after 1995, interferograms have less atmospheric effects and are well correlated.

Of the 29 two-pass interferograms made, 25 were selected to use in the SVD displacement velocity method. The number of usable interferograms was limited to 25 by the temporal span between the two SAR images used in the interferometry processing. Temporal spans of greater than 3 years would lead to decorrelation in the region of interest for this dataset. These 25 interferograms (Table 2.1) span the time from 1992 to 1997. Three of the two-pass interferograms used in the SVD analysis are shown in Figure 2.4. The interferograms in Table 2.1 were chosen due to their overlapping time spans with each other and with the ground water well data, high correlation values within the region of interest, and low amount of atmospheric affects. The SVD results are used in the storage coefficient calculation, and are compared with the 2-D gravity data.

2.3.2 AQUIFER STORAGE COEFFICIENT ESTIMATION

The storage coefficients for the Mimbres Basin were computed using the observed surface deformation from InSAR and groundwater level decline from five USGS well monitoring sites using the method used by my co-author, Krishnavikas Gudipati, in Buckley et al. (*in review*). Ground displacements were obtained from the average of nearest-neighbor InSAR pixels closest to each of the well locations. I plot the surface subsidence since 1992 and the groundwater depth vs. time (Figure 2.5). Multi-year average rate of change in water level are obtained from the slope of the linear trend fit to the data spanning from 1992 – 1997. The multi-year rate of change in surface displacement was obtained by dividing the cumulative, 1992-1997,

subsidence value by the number of years spanning these dates. A ratio of the rate of surface displacement to the water level change rate is equal to the storage coefficient because the coefficients are defined as total change in aquifer system compaction per change in head. The calculated storage coefficients of the five wells are given in Table 2.2.

2.3.3 GRAVITY DATA ANALYSIS

Bouguer gravity data from the Pan-American Center for Earth and Environmental Studies (PACES; http://paces.geo.utep.edu/) (Figure 2.6a) were used to determine the basin geometry. The bouguer gravity data were gridded in Geosoft Oasis Montaj software suite using a minimum curvature grid (Briggs, 1974) with 0.025° (2000 m) spacing. The grid was then geospatially transformed from latitude/longitude to UTM coordinates. This spatial transformation was done so the grid would be uniformly spaced. The transformed grid was high-pass filtered using the second vertical derivative method (Blakely, 1996) to remove the long wavelength signals associated with lower- and middle-crust structures (Figure 2.6b). By removing the long wavelength structures, small structures in the upper crust can be resolved in the gravity model. The filtered data were then scaled to units of eotvos (1 eotvos = $1x10^{-6}$ mGals/cm). This filtering process was completed using the Fugro-LCT program. LCT was used instead of Oasis Montaj due to its more sophisticated filtering package.

The filtered and rescaled gravity grid was used to produce a two-dimensional gravity model along a profile through the Mimbres Basin (Figure 2.7A). The gravity profile was modeled using GM-SYS. The gravity modeling process associates higher gravity values with denser material, and lower gravity values for less-dense material. However, gravity modeling is a non-unique geophysical tool in that many different models can represent the same area. Due to

this non-uniqueness, structural and stratigraphic constraints are necessary. The model presented here is constrained by work from Heywood (2002), Contaldo and Mueller (1991), and Mack et al., (1997). The model space spans depths from the surface, at 1.3 km above sea level (the mean elevation of Deming), to a depth of 120 m below sea level. The average density used for the upper unit of the basin filling sediments is 2,100 kg/m^3, which is consistent with interbedded layers of sandstone, shale, and alluvium (Sharma, 1997; Heywood, 2002). The lower unit was assigned a higher average density of 2,350 kg/m^3 due to the presence of clay-rich lacustrine deposits (Heywood, 2002). Thickness of each alluvial package was determined by work from Contaldo and Mueller (1991). Overall basin sediment thickness was taken from Heywood (2002), which estimates it from isostatic residual gravity anomalies, seismic reflection lines, and USGS exploration wells. The bedrock units underlying the basin fill sediments are assigned a density of 2,520 (Basement 1 in Figure 2.7b) and 2,600 kg/m^3 (Basement 2 in Figure 2.7B) (Sharma, 1997; Mack et al., 1997; Heywood, 2002). The Basement 1 density reflects the average density for fractured volcanic, mainly andesitic, units (Heywood, 2002). Basement 2 is consistent with average crustal densities composed of Paleozoic plutonic rocks of the Florida Mountains (Heywood, 2002). Since the lower- and middle-crust gravity anomaly have been removed during the filtering, small differences in upper crustal densities can be resolved

2.4 RESULTS

The InSAR analyses confirm that the observed surface deformation since 1992 coincides with the area of greatest historic groundwater level decline. The aquifer storage coefficients I calculate show that the aquifer is undergoing elastic deformation. The gravity analysis shows that the greatest amount of subsidence occurs in the deepest part of the Basin.

2.4.1 INSAR RESULTS

The deformation map in Figure 2.4 depicts a 15 x 11-km elliptical, asymmetric subsidence pattern in the north-central part of the Mimbres Basin. The deformation is located in the agricultural part of the basin just south of the city of Deming, NM, with the greatest amount of subsidence, 9.5 cm, captured at Well 7 over 5 years. The multi-year surface deformation patterns I observe correspond to the area of greatest historic groundwater level decline (Figures 2.2 and 2.4) (Contaldo and Mueller, 1991).

Also noticeable in Figure 2.4 is that the subsidence pattern is larger, both in areal extent and magnitude, after 1995 (Figure 2.4b-c) than prior to 1995 (Figure 2.4a). The growth of the deformation pattern is consistent with documented variations in local rainfall. This time period coincides with a period of moderate to severe drought during 1996 in southern NM as indicated by Palmer indices (NOAA, 2008). The Palmer index is a measure of cumulative, long-term drought conditions that takes into account hydrological and climatic conditions at large spatial scales (Palmer, 1965). The drought with continued pumping of the aquifer and lack of recharge to the aquifer leads to the large amount of observed surface subsidence during this time.

2.4.2 AQUIFER STORAGE COEFFICENT ESTIMATE RESULTS

The measured surface subsidence at each well (Table 2.2) gives a mean rate of 0.89 cm/yr in the period 1992 – 1997. The most rapid surface subsidence, 1.8 cm/yr at Well 7 (Table 2.2; Figure 2.1), is twice the rate of 0.9 cm/yr measured from leveling data over a period of 40 years at the same location by Contaldo and Mueller (1991). This suggests that there has been acceleration in the rate of ground subsidence since at least the early 1990s. The location of the

most rapid subsidence also coincides with the location of the greatest amount of historic water level decline (Figure 2.2). The average rate of water level decline is 1.14 m/yr (Table 2.2). This rate is 2.5 times larger than historic mean of ~0.44 m/yr measured by Contaldo and Mueller (1991) prior to 1990. These observations show that the rates of ground subsidence and groundwater level have increased in parts of the Mimbres Basin since 1992. These increased rates would be expected with the severe drought occurring during the mid-1990s. I suggest three hypotheses for this behavior in Section 2.5.

Holzer (1981) describes the relationship between groundwater level and subsidence at six areas located in Arizona, Texas, and California. This work groups the plotted linear relationship between subsidence and groundwater level decline into two groups: bilinear (two lines of different slopes), and linear (two lines of the same slope plotting on top of each other). A linear relationship would be indicative of a well-drained aquifer that is undergoing constant compressibility. A bilinear relationship can be the result of one or more of the following processes: (1) increases in the magnitude of seasonal groundwater level fluctuations with time; (2) time lags from slow drainage in fine grained beds; (3) increases in the thickness of the compacting sediment units; and (4) overconsolidation, which occurs when the preconsolidation stress is greater than the overburden stress. Holzer (1981) argues that overconsolidation is the most significant factor influencing this bilinear relationship due to the other mechanisms not reconciling with the field data and resulting in inconsistencies with reported bed thicknesses and coefficients of consolidation. In Figure 2.5, all of the wells used in this study have a bilinear relationship with the InSAR surface deformation. This observed bilinear relationship is similar to the Eloy-Pinacho, Az, Houston – Galveston area, Tx, and Tulare – Wasco area, Ca. (Holzer, 1981; Land and Armstrong, 1985).

To quantitatively assess the stress state in the aquifer, an aquifer storage coefficient can be calculated from the InSAR-derived, multiyear, surface subsidence measurements. These coefficients can be used to determine whether compaction – and the resulting surface subsidence – in the basin is occurring elastically or inelastically. The style of compaction, elastic or inelastic, depends on whether the effective stress during the observed time period exceeded the preconsolidation stress level, the maximum stress experienced by the aquifer. If the effective stress exceeds the preconsolidation stress, then inelastic compaction has occurred. If the effective stress does not exceed the preconsolidation stress, then elastic compaction is occurring within the aquifer (Holzer, 1981).

One of two approaches can be taken in order to evaluate if the preconsolidation stress has been exceeded: (1) by matching storage coefficients to another aquifer with a similar hydro-geologic environment and known preconsolidation stress and storage coefficients; or (2) comparing calculated and known preconsolidation stresses for the aquifer being studied. The first approach was utilized in this study because there are no known preconsolidation stresses for this area.

I chose to compare the Mimbres Basin to the Tulare-Wasco area in California to determine if the calculated storage coefficients indicate elastic or inelastic stress conditions. The Tulare-Wasco area (Land and Armstrong, 1985) was chosen for its hydrologic similarity to the Mimbres Basin, including intensive irrigation for agriculture, and arid climate. Elastic and inelastic coefficients have been reported for the Tulare-Wasco Basin (Holzer, 1981). These coefficients are compared to the estimated storage coefficients for the Mimbres Basin (Table 2.2). The Mimbres Basin coefficients fall within the range of elastic storage coefficients (2.5×10^{-3} to $<12 \times 10^{-3}$) reported for the Tulare-Wasco area in California (Land and Armstrong, 1985).

It is therefore determined that all of stress levels in the Mimbres Basin are elastic for the time span given in this study.

2.4.3 GRAVITY RESULTS

Inflection points in the 2-D gravity data profile (Figure 2.7a) are associated with either faults or changes in sediment thickness (e.g., Sharma, 1997). Similarly, inflection points within an InSAR-derived profile of surface deformation can be associated to the geologic controls on the deformation. This analysis was performed for the Hueco Basin (Schiek et al., 2006; Buckley et al., *in review*), and inflection points in the gravity and interferometry profiles revealed the presence of subsurface normal faults.

For the Mimbres Basin, a visual comparison of the two identified points in the gravity profile (A and FMF in Figure 2.8a) and their corresponding locations in the surface deformation profiles (Figure 2.8b-c) show the geologic controls on the surface subsidence bowl. Point A, positioned at the center of the profiles, aligns the deepest part of the basin (Figure 2.7b) with the deepest part of the subsidence bowl (Figure 2.8b) and the fastest rate of subsidence (Figure 2.8c). This correlation indicates that the greatest amount of subsidence occurs in the deepest part of the basin, where the upper and lower sediment packages are at their maximum thicknesses. Also notable in the profiles is the difference in the subsidence rate to the east and west of Point A. To the east of Point A, a maximum rate of 11 mm/yr of subsidence is observed over a 5-year period. However, to the west, a maximum of 17 mm/yr of subsidence occurs over the same time period. This difference of 6 mm/yr in the subsidence rates could be due to the existence of a thick lacustrine clay deposit in the deepest part of the basin.

The inflection point in the gravity profile corresponding to the FMF aligns with an area of decorrelation (Figure 2.8). To the east of the FMF, surface subsidence gradually decreases to approximately zero. This subsidence is likely due to compaction of alluvial fan sediment rather than deformation associated with the FMF because the rate obtained from the interferometry (~5 mm/yr) is unreasonably fast and far exceeds known Holocene slip rates (0.3 mm/yr) for other faults in the southern Rio Grande Rift (Woodward, 1977). This gradual, as opposed to abrupt, decrease to zero is the result of a thin piedmont of modern alluvial fan sediment at the edge of the Mimbres basin.

2.5 DISCUSSION

Visual integration of the interferometry, gravity, and storage coefficient results implies that faster deformation rates occur where the basin reaches its maximum depth, in the vicinity of Well 7 (Figure 2.9). Earth fissures surround this area. Since the area within the fissures is subsiding faster, ~10 mm/yr, than the surrounding area at ~8.5 mm/yr, tension cracks, or fissures, form in order to compensate for the change in subsidence rate (Haneberg, 1995).

There are two possible causes for the greater amount of ground subsidence at Well 7 than at the other wells (Figure 2.5). One possibility is that a greater amount of compaction is occurring at Well 7 than at Wells 3, 4, and 6. This is possible due to Well 7 being located in the deepest part of the basin, where the greatest amount of lacustrine clays also occurs (Figures 2.1, 2.7, 2.8, and 2.9). Cavity filling could result in higher deformation rates due to sediment compaction and filling of subsurface void space (O'Donnell et al., 2001). If present, a cavity could be the result of cooling fractures within the basaltic and andesitic volcanics comprised in

the upper layers of the basement (Heywood, 2002). Outside of the high deforming area, the basin is deforming uniformly, as shown by the storage coefficient analysis (Figure 2.9).

2.6 CONCLUSION

By integrating InSAR, gravity, and estimation of storage coefficients, an area within the Mimbres Basin can be defined that is subsiding at a faster rate (17 mm/yr) than the surrounding parts of the basin. The rapidly-subsiding part of the basin is outlined by mode 2 (Haneberg and Friesen, 1995) surface fissures (Figure 2.9). Although this area is subsiding at a faster rate, all of the Mimbres Basin is compacting elastically. Two possible explanations are given for the existence of the 17 mm/yr subsidence bowl: (1) a greater amount of compaction in lacustrine clays in this area; and (2) subterranean cavity filling in this area. With the available data, it is not possible to determine which of the two hypotheses is correct because the gravity data used does not have the resolution to image thin strata. Well log data could be used to test the two hypotheses by constraining the type, thickness, and depth of clay deposits that could contribute to the differing subsidence rates. However, no such data exists for the water wells in the study area. In the absence of well data, further geophysical work employing microgravity and high-resolution seismic surveys may be able to better image detailed basin stratigraphy and architecture, including the presence of cavities and lacustrine deposits.

2.7 ACKNOWLEDGEMENTS

I am grateful for the gravity data processing expertise provided by Dr. Ed Biegert (Shell Oil Company) and Ms. Holly Hunter-Huston (Hunter 3-D, Inc.). I would also like to thank Dochul Yang for his skills in InSAR processing. This work was funded by NASA grant NNG04GR42G.

2.8 REFERENCES

Anderssohn, J., Wetzel, H., Walter, T.R., Motagh, M., Djamour, Y., Kaufmann, H., 2008, *Geophysical Journal International*, vol. 174, no. 1, p. 287-294.

Amelung, F., Galloway, D.L., Bell, J.W., Zebker, H.A., Laczniak, R.J., 1999, Sensing the ups and downs of Las Vegas: InSAR reveals structural control of land subsidence and aquifer-system deformation. *Geology*, vol. 27, p. 483-486.

Berardino, P., Fornaro, G., Lanari, R., Sansosti, E., 2002, A new algorithm for surface deformation monitoring based on small baseline differential SAR interferograms. *IEEE Transactions on Geosciences and Remote Sensing*, vol. 40, no. 11, 2375–2383.

Blakely, R.J., 1996, Potential Theory in Gravity & Magnetic Applications: Cambridge University Press, Cambridge, UK.

Briggs, I.C., 1974, Machine contouring using minimum curvature. *Geophysics*, vol. 39, no. 1, p. 39-48.

Buckley, S.M., Gudipati, K., Schiek, C.G., Leuro, E., and Hurtado, J.M. (Jr.), in review (*Journal of Hydrology*), Ground deformation measurements and Hueco Bolson aquifer properties near El Paso, Texas from radar interferometry and gravity.

Buckley, S.M., 2000, Radar Interferometry Measurement of Land Subsidence, Ph.D. Thesis, University of Texas at Austin.

Bürgmann, R., Rosen, P.A., and Fielding, E.J., 2000, Synthetic aperture radar interferometry to measure Earth's surface topography and its deformation: *Annual Reviews of Earth and Planetary Science*, v. 28, p. 169-209.

Cabral-Cano, E., Dixon, T.H., Miralles-Wilhelm, F., Diaz-Molina, O., Sanchez-Zamora, O., Carande, R.E., 2008, Space geodetic imaging of rapid ground subsidence in Mexico City. *Geological Society of America Bulletin*, vol. 120, no. 11-12, p.1556-1566,

Contaldo, G.J., and Mueller, J.E., 1991, Earth Fissures of the Mimbres basin. NM *Geology*, vol. 13, no.4, p. 69-74.

Darton, N.H., 1915, Underground water of Luna County, NM. United States Geological Survey Water Supply Paper 345-C, p. 25-40.

Darton, N.H., 1916, Underground water of Luna County, NM. United States Geological Survey Bulletin 618.

Fetter, C.W., 2001, Applied Hydrology: New Jersey, Prentice-Hall, p. 598.

Galloway, D.L., Hudnut, K.W., Ingebritsen, S.E., Phillips, S.P., Peltzer, G., Rogez, F., Rosen, P.A., 1998, Detection of aquifer system compaction and land subsidence using interferometric synthetic aperture radar, Antelope Valley, Mojave Desert, California. *Water Resources Research*, vol. 34, p. 2573-2585.

Haneberg, W.C., Reynolds, C.B., and Reynolds, I.E., 1991, Geophysical characteristics of soil deformation associated with earth fissure near San Marcial and Deming, NM. *Land Subsidence (Proceedings of the Forth International Symposium on Land Subsidence, May 1991)*, IHAS Publ. no. 200.

Haneberg, W.C., and Friesen, R.L., 1995, Tilts, strains, and ground-water levels near an earth fissure in the Mimbres Basin, NM. *Bulletin of the Geological Society of America*, vol. 107, no. 3, p. 316-326.

Haneberg, W.C., 1995, Continuum Solutions for Draping and Differential Compaction of Compressible Elastic Layers – Implications for the origins and growth of Earth Fissures. U.S. Geological Survey Open-File Report 94-532, p. 63-65.

Heywood, C.E., Galloway, D.L., Stork, S.V., 2002, Ground displacement caused by aquifer-system water-level variations observed using interferometric synthetic aperture radar near Albuquerque, NM. United States Geological Survey Water-Resources Investigations Report, 02-4235.

Heywood, C.E., 2002, Estimation of alluvial-fill thickness in the Mimbres ground-water basin, NM, from Interpretation of isostatic residual gravity anomalies. United States Geological Survey Water-Resources Investigations Report 02-4007, p. 1-16.

Hoffmann, J., Zebker, H.A., Galloway, D.L., Amelung, F., 2001, Seasonal subsidence and rebound in Las Vegas Valley, Nevada, observed by synthetic aperture radar interferometry. *Water Resources Research*, vol. 37, no. 6, p. 1551-1566.

Holzer, T.L., 1981, Preconsolidation stress of aquifer systems in areas of induced land subsidence. *Water Resources Research*, vol. 17, p. 693-704.

Kim, S., Wdowinski, S., Dixon, T.H., Amelung, F., Won, J., Kim, J.W., 2008, InSAR-based mapping of surface subsidence in Mokpo City, Korea, using JERS-1 and ENVISAT SAR data. *Earth, Planets and Space*, vol. 60, no. 5, p. 453-461.

Lu, Z., Kwoun, O., and Rykhus, R., 2007, Interferometric synthetic aperture radar (InSAR): Its past, present and future. *Photogrammetric Engineering and Remote Sensing*, vol. 73, p. 217-221.

Land, L.F., Armstrong, C.A., 1985, A preliminary assessment of land-surface subsidence in the El Paso area, Texas. United States Geological Survey Water Resources Investigations Report, p. 85-4155.

Mack, G.H., Love, D.W., and Seager, W.R., 1997, Spillover models for axial rivers in regions of continental extension: the Rio Mimbres and Rio Grande in the southern Rio Grande rift, USA. *Sedimentlogy*, vol. 44, p. 637 – 652.

Massonnet, D., Feigl, K.L., 1998, Radar interferometry and its application to changes in the Earth's surface. *Reviews of Geophysics,* vol. 36, no. 4, p. 441-500.

Massonnet, D., Feigl, K.L., 1995, Discrimination of geophysical phenomena in satellite radar interferograms. *Geophysical Research Letters*, vol. 22, no. 12, p. 1537-1540.

McLean, J.S., 1977, Hydrologic maps and data in the Mimbres Basin, NM. United States Geological Survey Open-file Report 77.

NOAA, 2008, Historic Palmer Drought Indices: http://www.ncdc.noaa.gov/oa/climate/research/drought/palmer-maps.

O'Donnel, T.M., Jr., Miller, K.C., and Witcher, J.C., 2001, A seismic and gravity study of the McGregor geothermal system, southern NM. *Geophysics*, vol. 66, no. 4, p. 1002-1014.

Palmer, W.C., 1965, Meteorological drought. Research Paper No. 45, U.S. Weather Bureau.

Price, E.J., and Sandwell, D.T., 1998, Small-scale deformations associated with the 1992 Landers, California, earthquake mapped by synthetic aperture radar interferometry phase gradients. *Journal of Geophysical Research*, vol. 103, no. B11, p. 27,001-27,016.

Schiek, C.G., Luero, E, Buckley, S., and Hurtado, J., 2006, Characterization of anthropogenic land subsidence, its relation to fault system geometry, and their consequences for water table position in the El Paso, Texas area, using InSAR and gravity. *Eos Transactions American Geophysical Union,* vol. 87, no. 52, Fall Meeting Supplement, Abstract G43B-0999.

Sharma, P.V., 1997, Environmental and Engineering Geophysics: Cambridge, UK, Cambridge University Press, p. 475.

Theis, C.V., 1938, Progress report on the ground-water supply of the Mimbres Valley, NM. In: NM State Engr. 12th and 13th Biennial Reports, p. 135-153.

Wilson, B., 1985, Water use in NM in 1985. NM State Engineering Technical Report 46.

Woodward, L., 1977, Rate of crustal extension across the Rio Grande Rift near Albuquerque, New Mexico. *Geology*, vol. 5, no. 5, p. 269-272.

Valentine, D.W., Densmore, J.N., Galloway, D.L., Amelung, F., 2000, Use of InSAR to identify land-surface displacements caused by aquifer-system compaction in the Paso Robles area, San Luis Obispo County, California, March to August 1997. United States Geological Survey Open File Report, 00-447.

Zebker, H.A., Rosen, P.A., Goldstein, R.M., Gabriel, A., Werner, C.L., 1994, On the derivation of coseismic displacement fields using differential radar interferometry: The Landers earthquake. *Journal of Geophysical Research*, vol. 99, no. 19, p. 617-19,634.

Table 2.1: Interferograms used in SVD velocity displacement analysis. SAR images were acquired from a descending orbit.

Start Date	End Date	$Baseline_{perp}$ (m)	Time Span (days)
8/21/1992	4/23/1993	581	245
4/23/1993	9/10/1993	101	140
9/10/1993	7/30/1995	-413	688
7/30/1995	3/17/1997	-449	596
11/12/1995	1/21/1996	-272	70
11/12/1995	3/17/1997	-292	491
11/12/1995	1/6/1997	-360	421
11/13/1995	1/21/1996	70	69
11/13/1995	3/31/1996	-197	139
11/13/1995	1/6/1997	-18	420
11/13/1995	3/17/1997	50	490
12/17/1995	5/5/1996	164	140
12/17/1995	10/28/1996	307	316
1/21/1996	3/31/1996	-267	70
1/21/1996	1/6/1997	-88	351
1/21/1996	3/17/1997	-20	421
3/31/1996	4/1/1996	-115	1
3/31/1996	1/6/1997	179	281
3/31/1996	2/10/1997	-317	316
3/31/1996	3/17/1997	247	351
4/1/1996	1/6/1997	294	280
4/1/1996	2/10/1997	-202	315
4/1/1996	3/17/1997	362	350
1/6/1997	11/17/1997	321	315
3/17/1997	11/17/1997	253	245

Table 2.2: Elastic storage coefficients calculated from ratio of subsidence rate to groundwater level decline rate.

Well	Subsidence rate (cm/yr)	Water level decline rate (m/yr)	Aquifer storage coefficient
3	-0.74	-1.5	5.1×10^{-3}
4	-0.74	-0.99	7.5×10^{-3}
5	-0.83	1.2	-6.9×10^{-3}
6	-0.83	-0.99	8.4×10^{-3}
7	-1.8	-1.1	16×10^{-3}

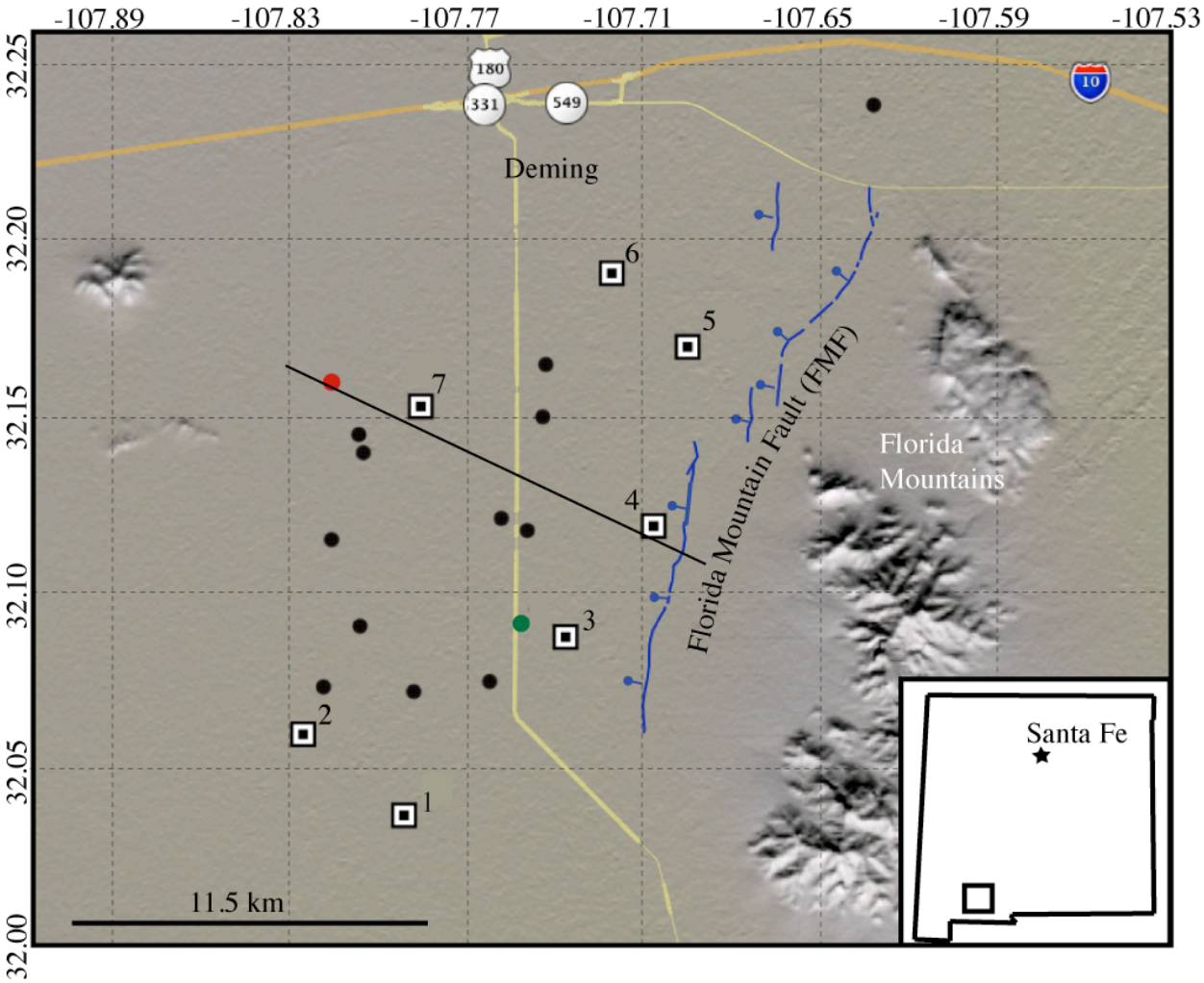

Figure 2.1: Map of the Deming, NM. Inset shows study area location. Blue line is the Florida Mountain Fault. Fault traces were obtained from the USGS Quaternary Fault and Fold Database of the United States (http://earthquake.usgs.gov/regional/qfaults/). Squares are groundwater well locations. Dots are earth fissures. Green dot is earth fissure shown in Figure 2.3a. Red dot is earth fissure shown in Figure 2.3b. Black line is approximate location of gravity and InSAR profiles.

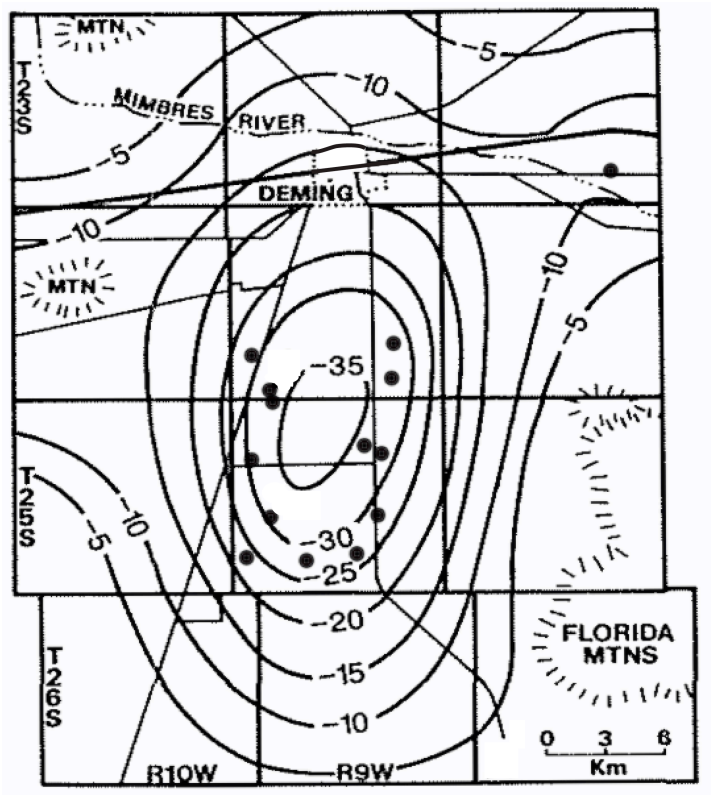

Figure 2.2: Water level decline from 1910 to 1990. Black dots indicate earth fissure locations. Contours are in meters. From Contaldo and Mueller (1991).

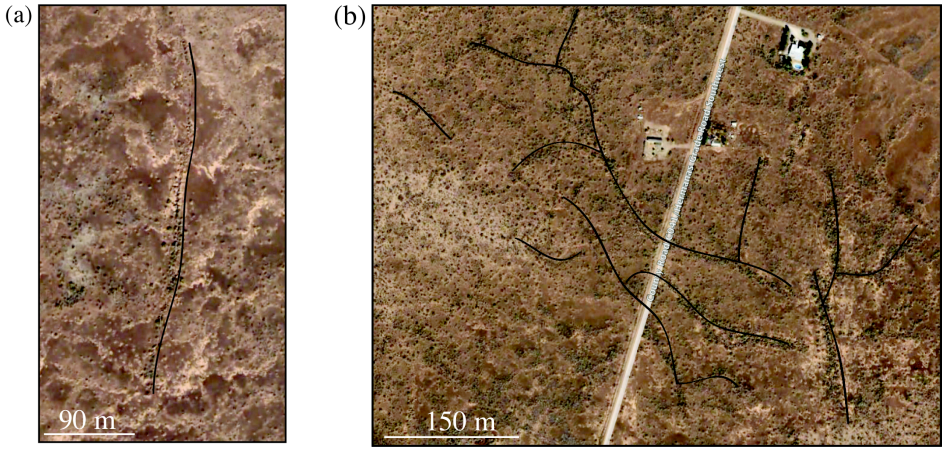

Figure 2.3: (a) Google Earth image depicting earth fissure (black line) curvilinear geometry. (b) Google Earth image showing orthogonal-polygonal earth fissure geometry.

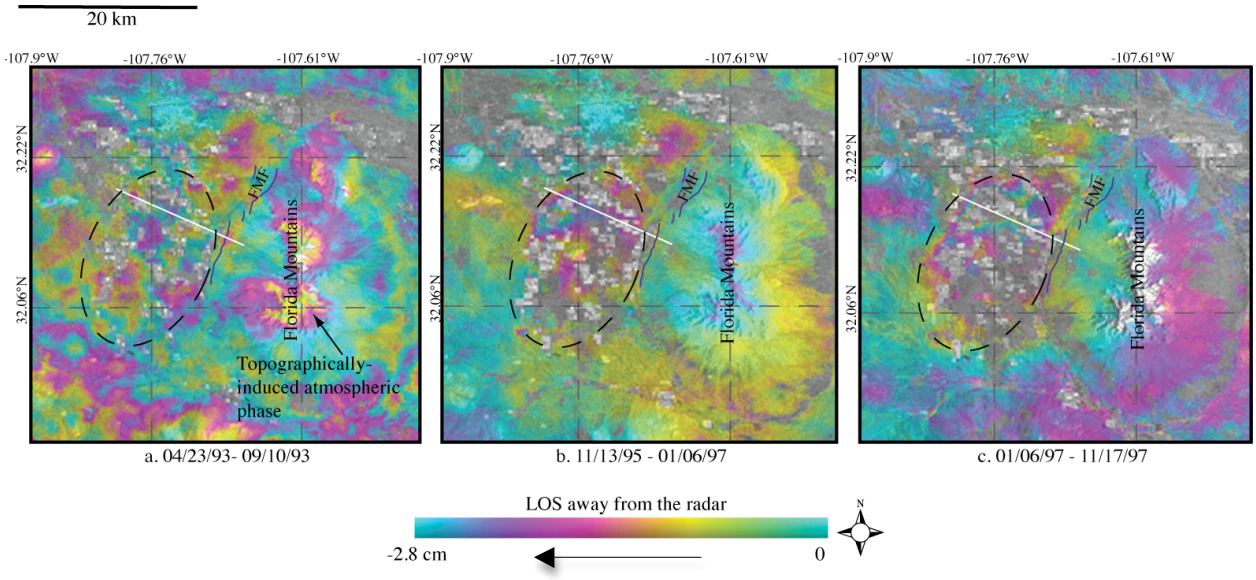

Figure 2.4: Flattened interferograms of the Mimbres Basin: (a) 04/23/93 – 09/10/93, (b) 11/13/95 – 01/06/97, (c) 01/06/97 – 11/17/97. White line indicates the trace of the surface subsidence profile shown in Figure 2.8. Black dashed ellipse is the approximate outline of the observed subsidence feature. One full color fringe is equal to 2.8 cm of subsidence in the LOS of the radar satellite.

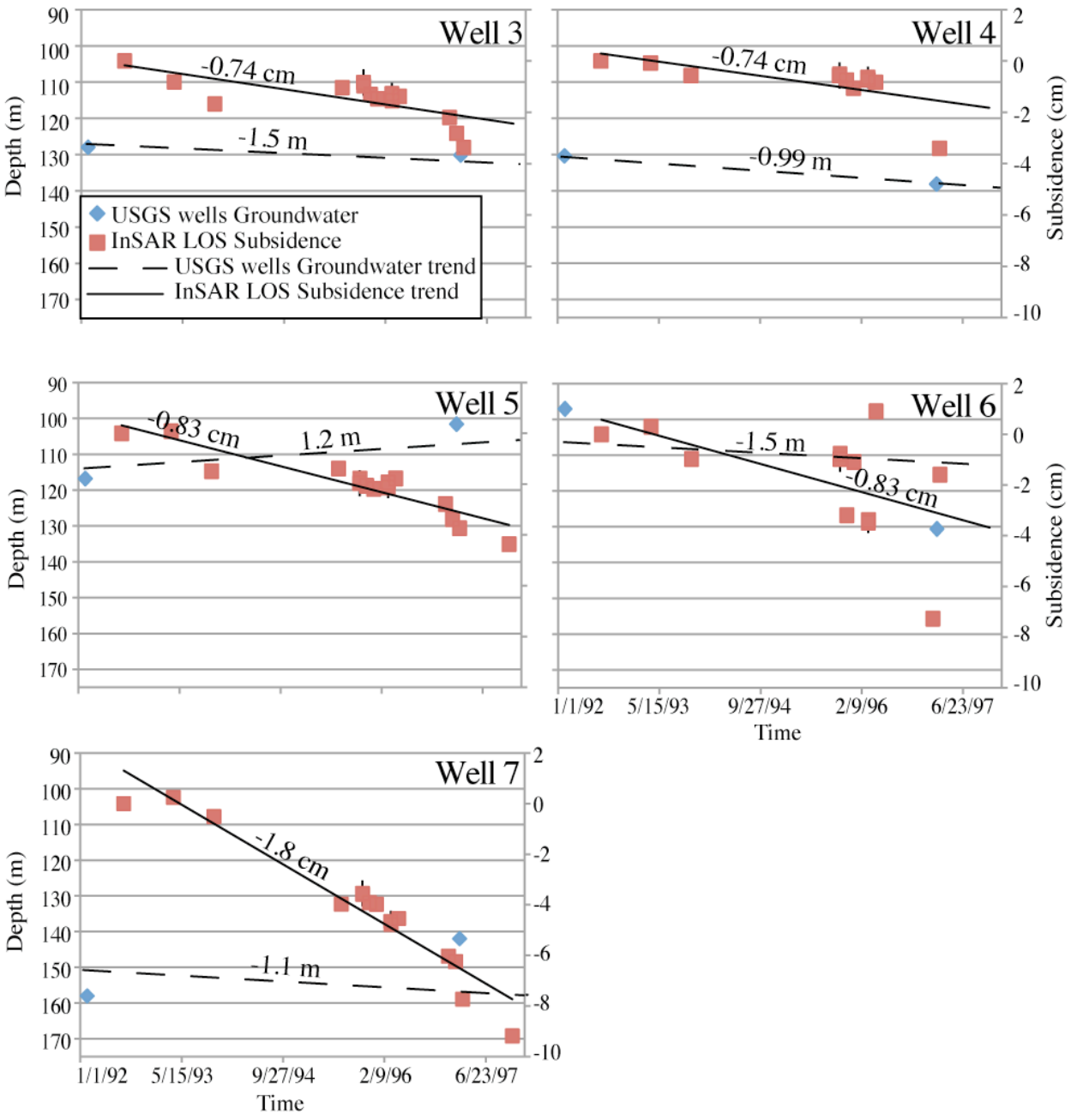

Figure 2.5: Comparison of USGS wells groundwater level (diamonds) and InSAR-derived LOS surface displacements (squares) changes at five well locations shown in Figure 2.1. Errors for subsidence values are shown at individual points. Slopes of the trend lines are given in Table 2.2.

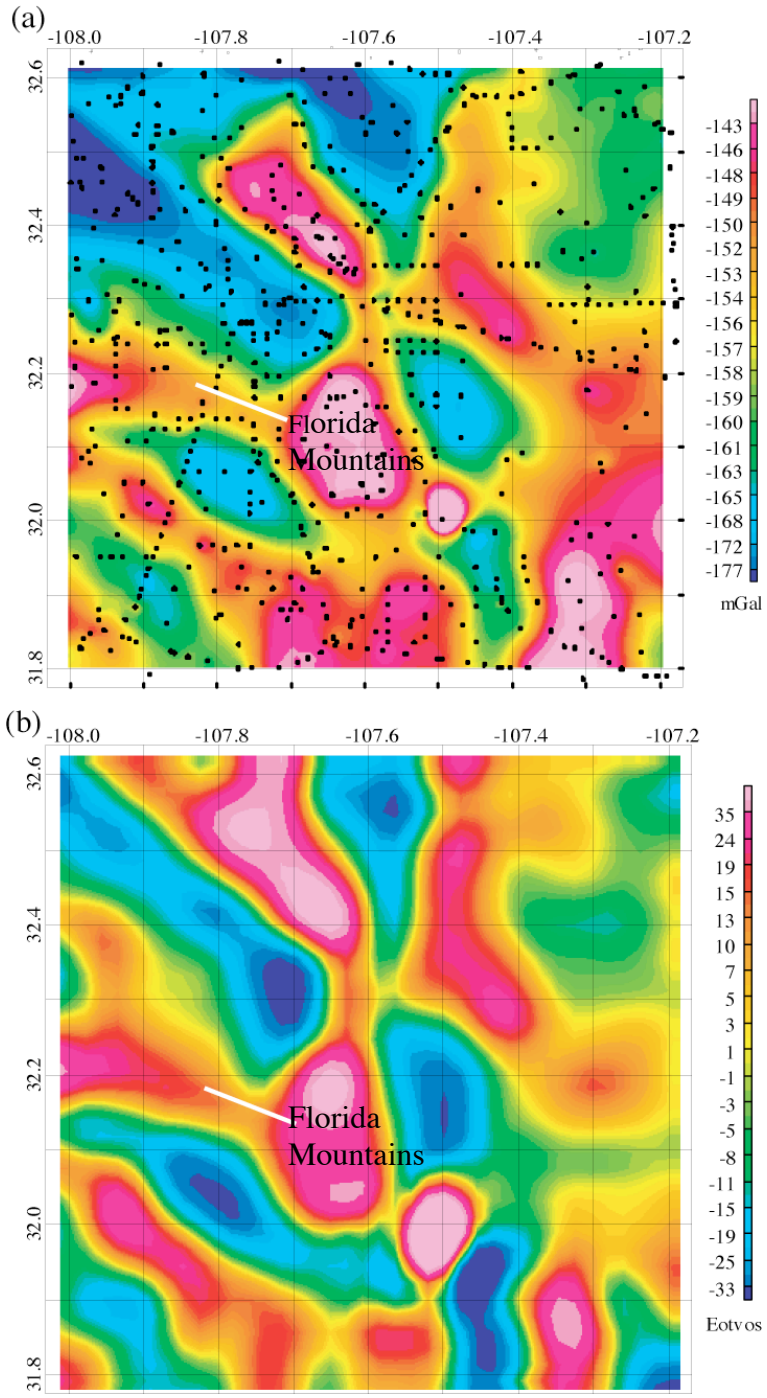

Figure 2.6: (a) Bouguer gravity anomaly map. Data obtained from the Pan-American Center for Earth and Environmental Sciences (http://paces.geo.utep.edu/gdrp). Dots are data point locations used to create the Bouguer anomaly grid. (b) Second vertical derivative or high pass filtered (in eotvos) calculated from the Bouguer gravity anomaly map in (a). The white line represents the profile used for gravity models shown in Figure 2.7 and 2.8. One eotvos equals $1x10^{-6}$ mGals/cm.

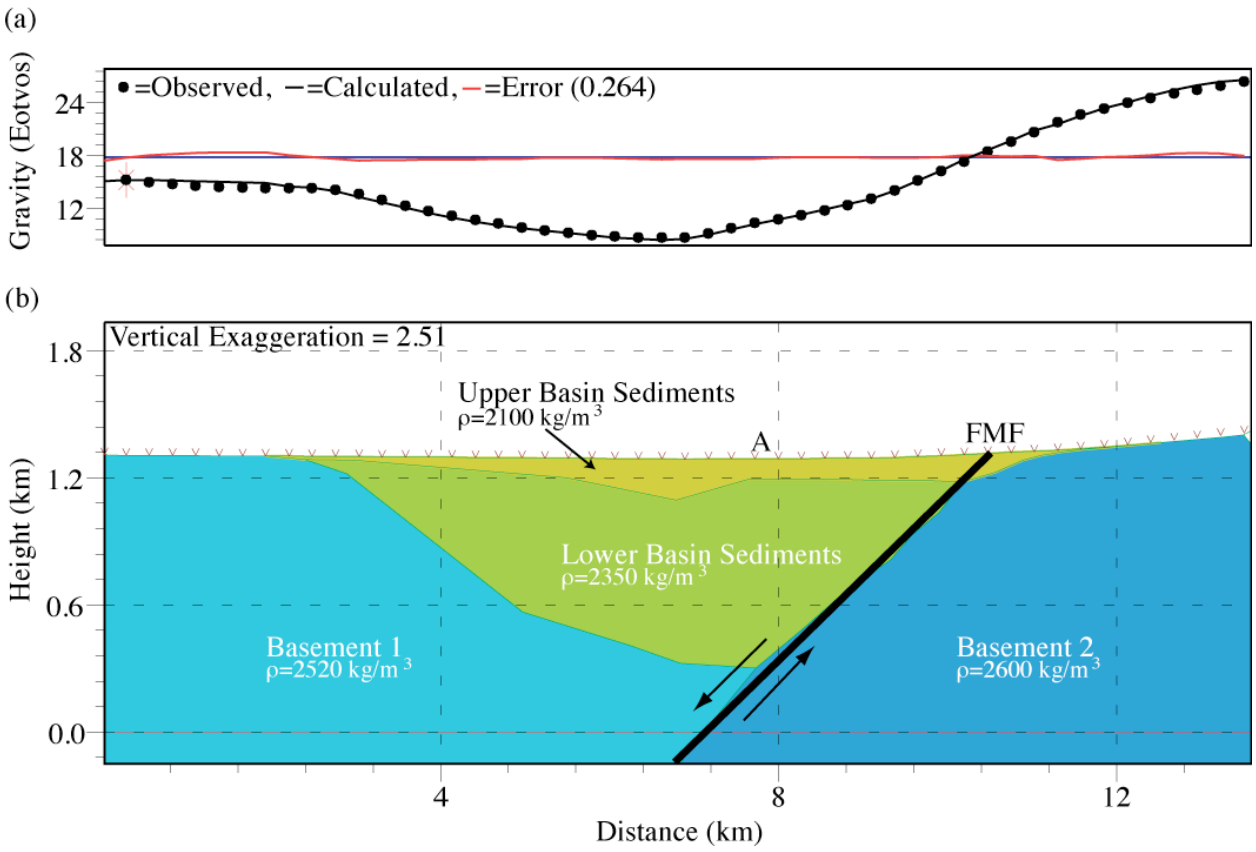

Figure 2.7: (a) Gravity profile from white line in Figure 2.6b. Points are the observed measured gravity. Black line is the gravity calculated from the model shown in (b). Red line is the error (observed gravity – calculated gravity). (b) Two-dimensional gravity model for a profile (white line in Figure 2.6b) through the Mimbres Basin. Model parameters are based on work by Heywood (2002) and Mack et al., (1997). FMF = Florida Mountain Fault. A indicates location of Basin's maximum thickness.

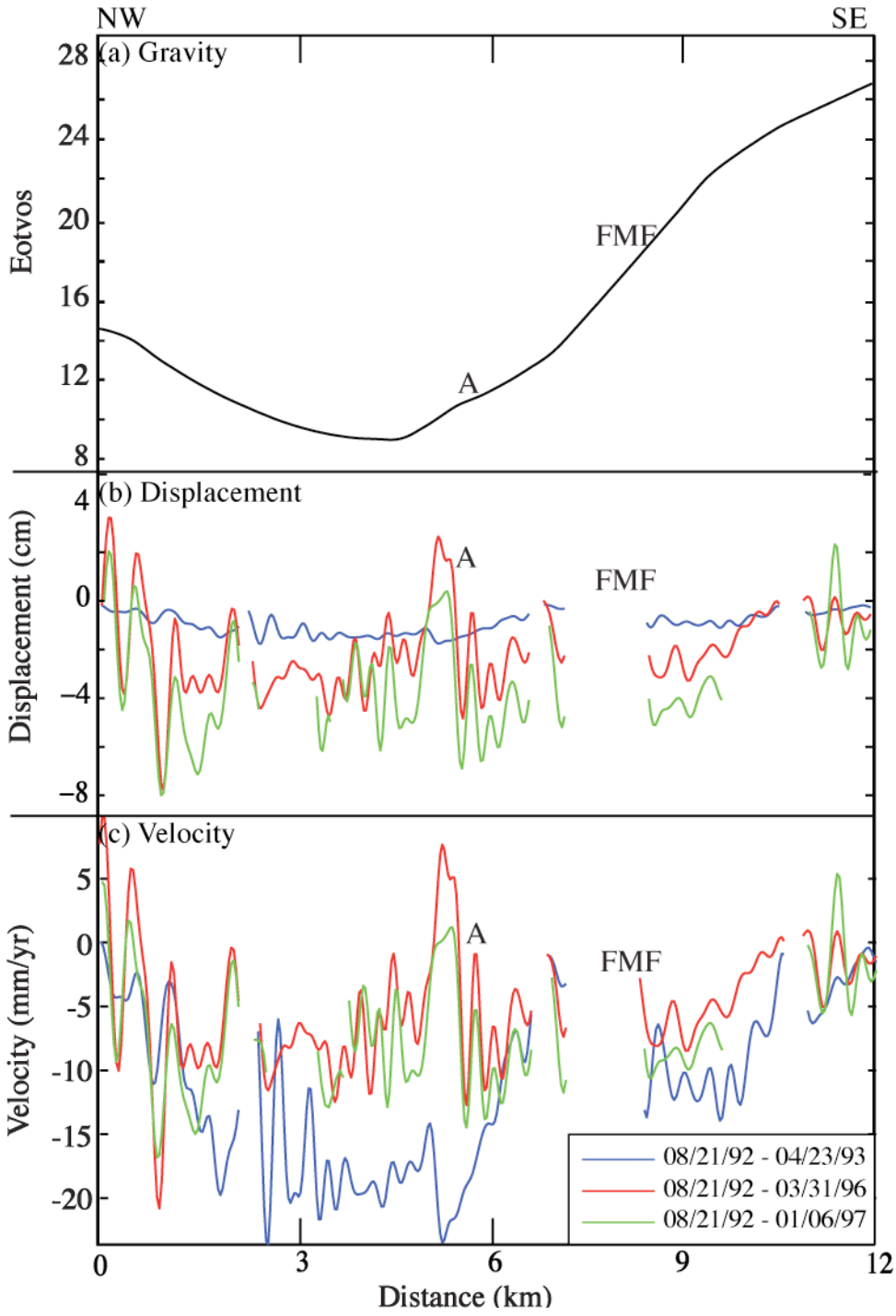

Figure 2.8: Comparison of gravity profile (top) from Figure 2.7a and InSAR-derived LOS surface displacement (middle) and velocity (bottom) profiles from Figure 2.4(a-c) derived the SVD velocity displacement technique. A is the basin maximum thickness. FMF corresponds to the location of the Florida Mountain Fault.

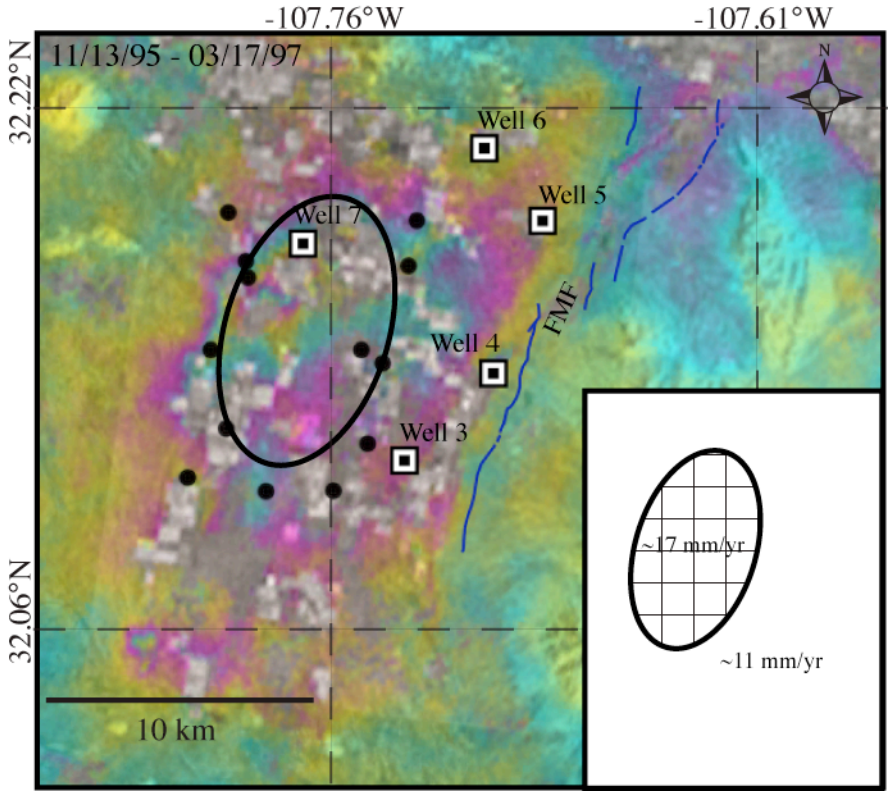

Figure 2.9: 11/13/95 – 03/17/97 interferogram with Earth fissure locations (black circles) and well locations (squares). Inset indicates areas of different subsidence rates. Oval on interferogram refer to area on inset. Same color scale is used as in Figure 2.4.

CHAPTER 3

DETERMINING VOLCANIC DEFORMATION AT SAN MIGUEL VOLCANO, EL SALVADOR BY INTEGRATING RADAR INTERFEROMETRY AND SEISMIC ANALYSES

ABSTRACT

From the early 1500s to the present day, San Miguel volcano has experienced at least 25 small eruptions, making it one of the most active volcanoes in the El Salvadoran volcanic chain. From 1867 to present, the volcano experienced, at most, 15 explosive, central vent eruptions with Volcano Explosivity Indices (VEI) of 1 or 2. To understand the explosive volcanism, I conduct an integrated geophysical study to determine which areas around the volcano are undergoing deformation that could lead to volcanic hazards, such as slope failure or flank lava flows. I analyze the volcanism by integrating Interferometric Synthetic Aperture Radar (InSAR) results with earthquake source and location data from a 10-month (March 2007-January 2008) seismic deployment. The InSAR results show a maximum of 11 cm of line of sight (LOS) volcanic inflation from March 2007 to mid-October 2007. During 12-18 October 2007, seismic activity increased to a Real-time Seismic-Amplitude Measurement (RSAM) value of >400. Normal RSAM values for this volcano are <50. A period of quiescence began in mid-October 2007, and a maximum of 7.5 cm of LOS deflation was observed in the interferometry results from mid-October to mid-January 2008. A cluster of at least 50 earthquakes that occurred between March 2007 and January 2008 define the seismogenic volcano-tectonic deformation located along the San Miguel Fracture Zone (SMFZ), a north-south fracture that cuts across the summit crater. I suggest that this activity is the result of magma and gas movement. The earthquakes in this zone were classified into four types, and among them gas movement is indicated by “Tectonic”

events, whereas magma movement is indicated by "Tremor" events. The earthquake cluster coincides with an area of surface deformation observed in the interferometry results. Surface deformation forward modeling was done using the geometry for the SMFZ inferred from the earthquake hypocenters to produce synthetic interferograms. A comparison between profiles from the synthetic interferograms, and the vertical component of deformation from the interferometry results shows that the vertical deformation is a likely result of fluid (e.g. gas, hydrothermal waters, and/or magma) overpressure along the SMFZ.

KEYWORDS: Radar Interferometry; InSAR; San Miguel volcano; El Salvador; volcano seismicity; volcanic tremor; Forward Model

3.1 INTRODUCTION

The San Miguel volcano lies within the Central American volcanic chain in eastern El Salvador (Figure 3.1). San Miguel most recently erupted in 2002 and prior explosive, central vent eruptions had Volcano Explosivity Indices (VEI) of 1 or 2 (GVN Bulletin, 2002; Perez et al., 2006). In October of both 2006 and 2007, the volcano experienced annual repetitive periods of heightened seismic activity (GVN Bulletin, 2006; GVN Bulletin, 2007). As of mid-October 2008, however, the volcano had not experienced any heightened seismic activity.

Considering the historically explosive and recently cyclic behavior of this volcano, it is critical to study the volcanic activity to assess the risk for the population, which is a mix of both urban and rural. The city of San Miguel, which lies on the northeastern flank of the volcano (Figure 3.1), has a population of ~150,000 and is the economic center of eastern El Salvador (Perez et al., 2006). The Pan-American and Coastal highways also cross the northern and southern flanks of the volcano, and a major eruption could devastate this infrastructure while endangering the lives of the local residents.

I conduct an integrated geophysical study to determine which areas around the volcano are undergoing deformation that could lead to volcanic hazards, such as slope failure or lava flows. I synthesize results from radar interferometry and seismic data recorded from a temporary, six-station, broadband network deployed around San Miguel volcano (Figure 3.1). This seismic deployment was performed in collaboration with researchers from Servicio Nacional de Estudios Territoriales (SNET). The seismic network recorded continuously during approximately the same time, from March 2007 to January 2008. I use synthetic aperture radar (SAR) data acquired between February 2007 and January 2008 to do an interferometry analysis.

Using the seismic data and a first order surface deformation forward model, I developed synthetic interferograms that were compared to observed interferograms in order to show the interaction between subsurface and surface deformation. I conclude that the upwelling of material (e.g, gases, hydrothermal or magmatic fluids) at San Miguel occurs at the San Miguel Fracture Zone (SMFZ). This material is either released through the SMFZ or is stored in the southwestern slope of the volcano.

3.2 BACKGROUND

3.2.1 TECTONIC SETTING

The Central American volcanic arc occurs where the Cocos plate subducts under the Caribbean plate at a rate of 73-84 mm/yr in a northeast direction (Corti et al., 2005). At this portion of the arc, the subduction zone has a dip of 45-55° and a crustal thickness of 32-40 km (Carr, 1984). The arc in El Salvador is oblique to the Central American trench, and the El Salvador Fault Zone (ESFZ) accommodates the transpressional plate tectonic regime (Figure 3.1). The ESFZ comprises a pair of ~2 m.y., right-lateral strike slip faults that strike NW-SE, parallel to the trench and the volcanic arc (Corti et al., 2005). A continuous GPS survey has shown that 14 mm/yr of transcurrent movement is associated with the ESFZ (DeMets, 2001). Within the ESFZ, a central graben, known as the Median Trough, accommodates tensional en-echelon faulting and pull-apart basins. The faults in the Median Trough act as guides for fissure eruptions (Chesner et al., 2004; Corti et al., 2005; Agostini et al., 2006).

San Miguel volcano is located in the eastern portion of the Median Trough (Chesner et al., 2004; Agostini et al., 2006). It is believed that one of these en-echelon faults is the conduit for fissure eruptions at San Miguel, as well as other volcanoes in the Salvadorian chain (Chesner

et al., 2004; Agostini et al., 2006). East of San Miguel, the Median Trough is not well understood due to a lack of seismic activity, a lack of obvious surface geomorphology indicative of significant faulting, and limited access to the eastern portion of the country due to civil unrest (Corti et al., 2005; Agostini et al., 2006).

3.2.2 SAN MIGUEL VOLCANO

San Miguel volcano, known locally as Chaparrastique, is a symmetrical stratovolcano (Figure 3.1) (Chesner et al., 2002). The volcano is 2130-m high, with a summit crater ~600 m in diameter and ~340 m deep (Chesner et al., 2004). The most explosive eruption at San Miguel occurred in 1510 AD, the event that destroyed the formerly pointed peak and created the modern summit crater (Meyer-Abich, 1956).

The volcano is composed of numerous basaltic-andesite to basalt lava flows, spatter, and scoria (Chesner et al., 2004). There have been five recent lava flows that date from 1699 to 1867. These flows occur on the flanks of the volcano along known fractures or vents (Figure 3.1). Although it lacked lava flows, the last eruptive activity occurred in January 2002 and had a VEI of 1 (GVN Bulletin, 2002). This eruption was a central vent eruption with explosions and a gas plume (GVN Bulletin, 2002). During heightened activity in 2005, a fumarole formed in the central crater (GVN Bulletin, 2006).

The volcano has had three heightened periods of both volcano-tectonic (VT) and long-period (LP) seismic activity since the 2002 eruption. A VT event is defined as an impulsive event capturing both high and low frequencies with visible P and S phases (Lahr et al., 1994). A LP event is characterized by a weak, emergent P phase, an absent S phase, and only captures the lower frequencies (Lahr et al., 1994). The first period was in October of 2005, and consisted of

~70 VT events. In September 2005, there were fewer than 10 VT events (GVN Bulletin, 2006). This low seismic activity is common in the months prior to a pulse of heightened seismic activity (GVN Bulletin, 2006). A second period of heightened seismic activity occurred during June 2006 with > 45 VT earthquakes, > 7,500 LP earthquakes, and a Real-Time Seismic Amplitude Measurement (RSAM; Endo and Murray, 1991) of 45 units compared to a previous background value of 8 units (GVN Bulletin, 2006; GVN Bulletin, 2007). A RSAM value is the calculated average amplitude of earthquakes during a pre-determined period of time, usually ~10 minutes (Endo and Murray, 1991). Increases in RSAM compared over daily or monthly time scales can suggest the onset of a volcanic eruption. The June 2006 period of heightened RSAM value was followed by another period of high seismic activity on 9 October 2006 (GVN Bulletin, 2007). This one-day event had a RSAM of 200 units (Escobar, 2007). The most recent period of heightened seismic activity, with a RSAM > 400 units occurred between 12-18 October 2007 and were captured by our seismic deployment (Escobar, 2007).

During the 2005 and June 2006 period of heightened activity, a small amount of lahars or landsliding occurred. From September to November 2005, small landslides occurred within the crater and a lahar occurred on the northern flank during heavy summer monsoonal rainfall (GVN Bulletin, 2006). Landsliding occurred within the crater again from March to June 2006 and in the latter part of the October 2007 seismic event (Escobar, 2007).

3.2.3 INTERFEROMETRIC SYNTHETIC APERTURE RADAR (INSAR)

InSAR is a powerful tool that can be used to measure surface deformation associated with volcanic inflation and deflation. It has been successfully applied to volcanic areas such as Mauna Loa, Hawaii (Sandwell et al., 2007); Arenal, Costa Rica (Wadge et al., 2006); Socorro,

New Mexico (Fialko et al., 2001b); the Galapagos Islands (Yun et al., 2006; Manconi et al., 2007); Ischia Island (Italy) (Manzo et al., 2006); and Long Valley Caldera, California (Fialko et al., 2001b). InSAR uses synthetic aperture radar (SAR) data to measure line of sight (LOS) surface displacements, e.g., surface displacement in the range direction with respect to the radar. This displacement is determined by taking the difference in phase between two time-separated SAR images. The phase difference is a combination of five effects: (1) differences in the satellite orbit of the two input images; (2) systematic satellite and environmental noise; (3) atmospheric noise; (4) topography; and (5) ground deformation (Lu et al., 2007). An interferogram that primarily shows ground deformation can be obtained using a two-step process. The first step is to select appropriate image pairs for the analysis. One criterion is to use radar image pairs with small differences in their satellite separation perpendicular to the LOS, which is known as the baseline perpendicular ($B_{\perp}$) (Massonnet and Feigl, 1998). A second criterion is to use radar images containing little or no vegetation. This will reduce environmental noise that, for example, arises from changing vegetation patterns, and that often results in temporal decorrelation between radar image pairs, making interferograms difficult or impossible to use.

The second step in the interferometry processing is to isolate the deformation signal by removing the influence of topography in the interferogram (Bürgmann et al., 2000; Lu et al., 2007). Topography is removed by first using an accurate digital elevation model (DEM) and the imaging geometry of the input SAR images to generate a synthetic interferogram (Massonnet and Feigl, 1998). This synthetic interferogram is subtracted from the raw interferogram obtained from the input SAR images, resulting in a ground deformation interferogram. This processing was done using the Gamma Remote Sensing Interferometry package.

Volcano interferometry can include various effects resulting from topography. Such effects include topographically-induced atmosphere phase signals, layover, and shadow (Bürgmann et al., 2000; Massonnet and Feigl, 1998). Topographically-induced atmosphere artifacts are errors associated with variable gradients in water vapor, temperature, and pressure in the lower troposphere over mountainous areas (Delacourt et al., 1998). In an interferogram, this type of error produces fringes that mimic topographic contours and can result in 3π - 4π of extraneous phase in mountainous areas (Delacourt et al., 1998; Remy et al., 2001). This type of error can also be mistaken for true volcanic deformation. Layover is a geometry ranging effect due to the topographic slope exceeding the radar incidence angle (Bürgmann et al., 2000).

For my analyses, I use L-band SAR data from the Advanced Land Observing Satellite (ALOS) mission. The ALOS data is useful because microwave radiation at the L-band frequency (1.25 GHz; 23 cm wavelength) tends to penetrate the vegetation covering the San Miguel volcano. Table 3.1 gives the parameters for each interferometry pair used in this analysis. Processing details are given in Section 3.3.1. This data was provided by the Western North America Interferometric Synthetic Aperture Radar (WInSAR) Consortium hosted under UNAVCO.

3.2.4 SEISMIC DEPLOYMENT

SNET has monitored El Salvador for earthquakes and volcanic eruptions since the 1960s (Fernandez et al., 2004). From March 25, 2007 to January 20, 2008, the University of Texas at El Paso (UTEP) augmented the SNET seismic network in the vicinity of San Miguel with a continuously-recording, six-seismometer temporary network. The temporary deployment was configured to focus on the southern slope of San Miguel volcano (Figure 3.1), an area that has

been the site of an increased number of seismic events compared to the rest of the volcano during the past three episodes of seismic activity (Figure 3.2) (Escobar, 2007).

The UTEP network comprised of Gurlap, 40T and 3T, broadband seismometers. Four of the six seismometers were co-located with SNET 1Hz seismometers to ensure the equipment was housed in a secure location that coupled well with the ground. Three of the four co-located stations ("VSM", "LAC", and "BM") were located on the flanks of the volcano (Figure 3.1). These sites were equipped with Gurlap 40T seismometers. The fourth co-located station, "PAC," was located on the neighboring El Pacayal volcano, northwest of San Miguel volcano (Figure 3.1), and this site was equipped with a Gurlap 3T seismometer. Two additional Gurlap 3T instruments ("MAR" and "GPS") were placed on the south flank of the volcano (Figure 3.1). MAR was located in a Papaya orchard and GPS was co-located in a hut with a Global Positioning System (GPS) station operated by the University of Wisconsin.

The 3T instruments enabled us to record longer periods seismic signals, ~100 s, compared to the 30-s response of the 40T instruments (Gurlap, 2008). This longer seismic response afforded by the 3T seismometers is useful for studying long period volcanic tremor. All of the seismometers were powered by solar panels and car batteries. The data acquisition recorder (DAS) for each seismometer was a RefTech 130.

3.3 DATA PROCESSING AND RESULTS

I perform a radar interferometry analysis with Gamma Remote Sensing to determine the magnitude of inflation and/or deflation, and the spatial pattern of the volcanic deformation at San Miguel. I also process the raw seismic data from the temporary network using a combination of the Antelope Boulder Realtime technologies (BRTT) (BRTT, 2008), EvLOC (Bratt and Bache,

1987), HypoDD (Waldhauser and Ellsworth, 2000), and Seismic Analysis Code (SAC) (IRIS, 2008) software packages. I located and studied the source locations for the earthquakes using this approach.

3.3.1 INSAR DATA PROCESSING

A two-pass differential interferometry technique (Zebker et al., 1994) was applied to ALOS radar images (Table 3.1) of San Miguel volcano acquired between February 2007 and January 2008. Using the Gamma Remote Sensing Interferometry package, topography was removed from each resulting interferograms using a 90-m resolution Shuttle Radar Topography Mission (SRTM) DEM. The 90-m DEM was first resampled using bi-linear interpolation to 30-m resolution before being used in the InSAR analysis. This resampling was performed in order to have the DEM and SAR imagery at approximately the same spacing. This analysis gives a final set of four interferograms (Figure 3.3) spanning the time between February 2007 and January 2008. The two interferograms for the periods 03/03/07-10/19/07 and 10/19/07-01/19/08 are from a descending satellite track. The other two interferograms, for the time spans 02/27/07-10/15/07 and 10/15/07-01/15/08, are from an ascending satellite track.

Due to the amount of decorrelation present around the volcano (Figure 3.3b), an additional set of InSAR processing steps were explored to investigate whether correlation around San Miguel could be improved. These steps effectively shorten the time span between images, lessen the amount of $B_{\perp}$, and increase the correlation. This analysis used the following images: 02/27/2007, 08/30/2007, and 10/15/2007. The result of this processing shows a maximum of 5.8 cm of deformation between 02/27/2007-10/15/2007 on the cone, using only the 02/27/2007 and 10/15/2007 images. This is approximately the same to the amount of deformation, maximum of

6.1 cm, observed in the same time span after introducing the 08/30/2007 image. However, while the 02/27/2007-08/30/2007-10/15/2007 interferogram added coherence in some parts of the resulting interferogram, it did not add any extra coherence around San Miguel. For this reason, the 02/27/2007-10/15/2007 interferogram is used for the rest of the interpretation.

3.3.2 INSAR RESULTS

Figure 3.3 shows the LOS interferograms from the InSAR analysis. I find deformation to be occurring within the top portion of the cone. Profiles were acquired across the cone as shown in Figure 3.4. The profiles were chosen in order to focus on the southern slope of the volcano where most of the seismometers were deployed and where the magma chamber is thought to exist (Escobar, 2007). A maximum of 11 cm of inflation occurred before mid-October 2007 (Figure 3.3b). Between mid-October 2007 and mid-January 2008, a maximum of 7.5 cm of deflation occurs (Figures 3.3c and 3.4c). Both inflation and deflation are localized to the upper part of the cone and define a broad area that spans the top of San Miguel from southwest to northeast.

Profiles taken from the LOS deformation maps for San Miguel volcano indicate that the greatest amount of inflation and deflation occurred in the vicinity of the summit crater (Figure 3.4). Interestingly, the LOS profiles reveal deflation magnitudes have a mirrored symmetry to the inflation magnitudes (Figure 3.4). This mirrored symmetry suggests that inflation and deflation deformation arise from the same volcanic mechanism.

3.3.3 SEISMIC PROCESSING

The purpose of the seismic processing is to resolve relative earthquake locations from the collected raw seismic data and classify the type of events that occur in and around the volcano. The raw seismic data was first processed using Antelope (BRITT) software to achieve automated first arrival detections and events. These events are then relocated using a modified version of HypoDD (Ammon, 2008). The resulting earthquake locations are then classified into 4 groups to aid in finding regions of tectonic or volcanic deformation. A tutorial of the seismic processing is given in Appendix A.

3.3.3.1 Automated Detection

I use a short-term average window (STA) to long-term average window (LTA) automated detector to pick first arrivals on the continuous data using the Antelope (BRTT) software (e.g. Velasco et al., 2007; Velasco et al., 2008). For a detection to be made, the ratio between the STA and LTA must be greater than an empirically set signal to noise ratio (SNR). A 5-Hz highpass filter was used on the data to remove regional seismic events from the nearby subduction zone, thus focusing the detections on only local events (e.g. Velasco et al., 2007; Velasco et al., 2008). I adjusted the STA and LTA time windows to optimize the process of identifying both impulsive volcano-tectonic events and emergent tremors. The 5-Hz filter with 5-sec STA and 10-sec LTA windows was used for detecting first arrivals of both volcano-tectonic and volcanic-tremor. A SNR value of 3.0 was used to identify the detection.

Once the detections were made, the detections were associated to events on a grid of hypothetical locations (Velasco et al., 2007; Velasco et al., 2008). The detected P-wave must be observed in seismograms from at least four stations in order to be associated with an event.

Once an association is determined and an event is recorded, we locate the hypothetical events to relative geographic locations using EvLoc (Bratt and Bache, 1987). In the EvLoc calculation, we use the IASP91 standard earth velocity model (Kennett and Engdahl, 1991). This model includes a linear increase of velocity with depth (Kennett and Engdahl, 1991). I obtained 600 preliminary earthquake epicenters from this analysis. We refine our search of events by focusing on 57 events that occurred within the network.

3.3.3.2 Relative Earthquake Locations

To refine our epicentral locations determined from EvLoc, I use a modified version of the double-difference approach (HypoDD; Waldhauser and Ellsworth, 2000) that allows for constraints and weights on seed depths to control the amount of movement in the depth estimates for the singular value decomposition (SVD) approach (Ammon, 2008). The constraint parameter ranges between 0 and 10, with 0 indicating a tightly constrained depth and 10 an unconstrained depth. The weight parameter ranges between 0 and 10, with 10 indicating the highest possible weight given to a particular location in the model. Constraining and weighting the seed depths is performed because I do not have sufficient depth control to calculate an absolute depth for each earthquake location due to station aperture and the small number of stations in the temporary network. I also used the IASP91 standard earth velocity model (Kennett and Engdahl, 1991).

I tested the sensitivity of this modified HypoDD approach for depth estimation by running a series of tests using different seed depths (1 km, 1.5 km, 1.75 km, 2 km, 2.25 km, 2.5 km, 3 km, 4 km, 5km) and varying depth weights. The range of seed depths was chosen because SNET's continuous monitoring indicates the source of volcanic deformation lies within this depth range (Escobar, 2007). For each seed depth, we run unconstrained depths, and constrained

depths for weights of 5 and 7. Figure 3.5 shows the outcomes of the sensitivity testing. A constrained depth and weight of 5 allowed depths to vary within a ±1.5 km range (Figure 3.5a-i2), whereas a free depth and weight of 10 restricted variation in depth to a range of ±0.5 km (Figure 3.5a-i1). I found that a seed depth of 1.75 km with a constrained depth and weight of 7 matched the spread and depth of the historic data (Escobar, 2007), and thus these values give my preferred locations (Figure 3.5c3). Figure 3.6 shows the resulting relative earthquake epicenters plotted with the historic earthquake locations from SNET. The relative earthquake location results display a cluster of 57 earthquakes located along the SMFZ (Figures 3.1 and 3.6). These 57 earthquakes have an average epicentral upward propagation error (Taylor, 1982) of 4 km. The average error in depth is greater than 100 km. Given the depth uncertainty, I consider the depths to be only of limited value for my analysis.

The input files for this analysis is given in Appendix B. Input values were found empirically with the aid of example 3, Long Valley Caldera, given in the HypoDD program suite (Waldhauser, 2001). The file ph2dt.inp is used to categorize and control earthquake clustering. The other file listed in the appendix, hypodd.inp, is the control file for HypoDD. This file has the analysis types (e.g., SVD or least square), clustering parameters, correlation weighting values, and 1-D velocity model used in the calculation. The 1-D velocity model is directly taken from example 3 given in the HypoDD program suite (Waldhauser, 2001).

3.3.3.3 Earthquake Location Classification

From the 57 events, I calculated spectrograms for each earthquake and used them to classify each seismogram into an earthquake type. I found four distinct types of earthquakes in our dataset. The first, Type 1 or "Tectonic", is an event characterized by high frequencies (>15

Hz) and no background volcanic tremor (Figure 3.7a). I classified 9 events in this type. The second type, Type 2 or "Tectonic with Background Volcanic Tremor", is an event similar to the first with the addition of volcanic tremor as a background signal (Figure 3.7b). There are 16 events in this category. The third, Type 3 or "Tectonic with a Precursory event and Background Volcanic Tremor", is a high-frequency, tectonic event with both evidence of volcanic tremor and a precursory volcanic tremor event (Figure 3.7c). There are 6 events of this type in the dataset. The last category is "Volcanic Tremor," Type 4, (Figure 3.7d) (Cramer and McNutt, 1997). These events are emergent, low- to moderate-frequencies, (2-10 Hz), with durations greater than 10 sec, and have multiple pulses. The majority of the events in the catalog are of Type 4, with a total of 26 events. The spatial distribution of the classified events is shown in Figure 3.8.

3.3.3.4 Local Magnitude

Local magnitudes were calculated for event Types 1, 2, and 3 using a method by Stein and Wysession (2003). Type 4 events were not included in this magnitude calculation due to the ambiguity in the P-arrival pick for an emergent tremor signal. First, displacement seismograms were calculated from the raw data. The displacement seismograms were then converted to Wood-Anderson displacement seismograms (Stein and Wysession, 2003). A local magnitude (M_L) is calculated using the Wood-Anderson displacement seismogram and the following relationship:

$$M_L = \log(A) + 2.76\log(\Delta) - 2.48 \qquad (3.1),$$

where A is the maximum amplitude in the Wood-Anderson displacement seismogram, and Δ is the distance from the source to the receiver in kilometers. Calculated M_L for the earthquakes are given in Table 3.2 and Figure 3.9.

3.3.4 SEISMIC PROCESSING RESULTS

The earthquake locations and historic SNET data (Figure 3.8) show that the earthquake locations occurred along a linear trend closely aligned with the SMFZ (Figure 3.1) and not in a circular cluster. The locations that are scattered to the west of SMFZ are mostly type 4 earthquakes, which can be attributed to magma and (or) gas movement from the SMFZ into the volcano's southern slope (Figure 3.8). In map-view, a ~1-km diameter zone at the summit of San Miguel can be defined. It is relatively devoid of events and surrounded by a large amount of seismic activity (Figure 3.8). In cross-section, this zone is associated with a subsurface structure, also characterized by few events surrounded by a high density of events, that spans depths from the approximately 1 to 2 km (Figure 3.8d).

Seismic activity on the northern slope of San Miguel consists of all four-event types, and, interestingly, this is the only place where Type 3 events occur (Figure 3.8b). On the southern slope of San Miguel, seismic activity includes Types 1, 2, and 4 (Figure 3.8c). Calculated magnitudes display most earthquakes with >3.5 M_L occur east of the SMFZ (Figure 3.9). Type 2 events have the highest average magnitude at 2.79 (Table 3.2). Types 1 and 3 have average magnitudes of 2.69.

3.4 DISCUSSION

To examine the relationship between the earthquake locations and surface deformation, forward modeling of the inflation that occurred before mid-October 2007 and the deflation that occurred after mid-October 2007 was performed. For the forward modeling process, I utilized the MATLAB program called the Synthetic Interferogram Calculator (SIC) (Fialko, 2001a)

kindly provided by Professor Yuri Fialko at the University of California at San Diego. Given a subsurface deformation source, SIC will compute a predicted surface deformation field. SIC can forward model a Mogi-type point source (Mogi, 1958), Yang prolate sphere source (Yang et al., 1988), Fialko penny-shaped crack (Fialko et al., 2001a). The Mogi, Yang, and Fialko models are used for volcanic modeling. These models have been used at Campi Flegrei caldera, Italy (Gottsmann et al., 2006); Long Valley Caldera, CA (Fialko et al., 2001b; Newmann et al., 2006); Galapagos Islands (Yun et al., 2006; Manconi et al., 2007); and Socorro, NM (Fialko et al., 2001b).

The three volcanic modeling sources differ by their source geometry. All three-source types either contract or expend from a change in pressure (Δp), known as the excess magma pressure (Gottsmann et al., 2006). The Mogi and Yang source geometries represent different types of spheroid magma chamber shapes. The Mogi-type point source is defined as a spherical-body. The Yang source has a prolate spheroid geometry. The Fialko source has the geometry of a sill in the shape of a flat disc.

For San Miguel, the Mogi, Yang, and Fialko models were run in SIC and the results were compared to determine which model best captures the magnitude and wavelength of the InSAR-observed LOS deformation. To determine the correct usage of the SIC model input variables, I reproduced the Yang model in Newmann et al. (2006). In completing this exercise, I found that: SIC requires depths measured from the surface to center of the source; the strike of the major axis is assumed to be measured clockwise from north; and a horizontal axis is defined to have zero dip.

The parameters for each model are given in Table 3.3. Satellite parameters including the look angle, azimuth (heading measured clockwise from north), and SAR radar wavelength were

obtained from the interferogram parameter files. The shear modulus and Poisson ratio used in the model are typical values for volcanic areas (Fialko et al., 2001a; Fialko et al., 2001b; Gottsmann et al., 2006; Newmann et al., 2006). Each model was constructed on a 5 x 5 km grid using 30 m spacing. The subsurface geometries used for each model were taken from the seismic analysis results (Figure 3.8), as well as field and petrologic observations from Chesner et al. (2004). Since the seismic analysis resulted in preliminary depths, the field, and petrologic observations from Chesner et al. (2004) locate the magma chamber near the southern slope of the volcano at a depth of 600 m, which would place the top of the chamber ~90 m under the summit crater. Using an upward bound of 600 m and lower bound of 1.5 m (Figure 3.8) for depth values, I empirically find that 600 m is the best depth estimate giving the best approximate wavelength in deformation profile (Figure 3.4).

A critical parameter in Table 3.3 is the excess magma pressure, Δp. A maximum excess magma pressure ($\Delta p_{\max}$) is calculated in order to give an upper limit to this variable. The $\Delta p_{\max}$ is the assumed maximum pressure in the chamber, and is equal to the lithostatic pressure by this relationship (Gottsmann et al., 2006; Newmann et al., 2006):

$$\Delta p_{\max} = \frac{\Delta V \mu}{\pi a_{\min}^{3}} = \left(d - a_{\min}\right)\rho g \qquad (3.2),$$

where ΔV is the minimum volume change measured from InSAR observations, μ is the shear modulus, $a_{\min}$ is the minimum radius for the spheroid source, d is the magma chamber depth, ρ the density of the surrounding solid rock, and g is gravity (9.8 m/s^2). Using the values in Table 3.3 in eq. 3.2, $\Delta p_{\max}$ is 42 MPa. If Δp becomes greater than the $\Delta p_{\max}$, then an eruption will occur. In order to estimate the excess magma pressure for the inflationary or deflationary event captured by each interferogram, Δp for the corresponding models (Mogi, Yang, and Fialko)

were resolved empirically. This was done by changing the Δp value until the maximum magnitude of modeled deformation was equal to the maximum observed deformation. Each of the resulting, modeled Δp values is below Δp_{max} (Table 3.3).

Figure 3.4 shows the four InSAR-derived LOS deformation profiles, and, for each interferogram, the three modeled LOS deformation profiles are also shown. Comparison of the models and InSAR profiles reveal that any of the generated models could easily produce the surface deformation. Upon closer inspection using a Root Mean Square (RMS) error calculation (Taylor, 1982), the Yang model gives a smaller residual error than the other models (Table 3.4). Since the Yang model gives the best approximation, this will be the source model used to make the synthetic interferograms (Figure 3.10). Each synthetic interferogram is compared to its corresponding InSAR-derived displacement map. Residual maps were calculated for displacement map-synthetic interferogram pair (Figure 3.10). The residuals for models shown Figure 3.10a and b have an error range of <±1.5 cm on the upper portion of the cone, and >±2 cm on the lower portions of the cone. For a first order surface deformation model, this is an acceptable amount of residual errors when compared to anticipate topographically-induced atmospheric effects. Interestingly, the residual for the 03/03/2007 – 10/19/2007 interferogram (Figure 3.10b) shows positive residuals to the east of the summit and negative residuals to the west of the summit. One interpretation is that the residual is the result of tectonic movement along a north-south striking normal fault (the SMFZ) that was not considered in the inflationary models. The majority of tectonic events during our seismic deployment occur from October 12, 2007 to Oct. 19, 2007. Because the 03/03/2007 – 10/19/2007 interferogram is the only one to span that time, it is the only that captured the tectonic deformation represented in the residual.

Unfortunately, this residual could not be modeled because parameters such as fault rupture length are unknown for the event.

From the model and interferometry results, an observed 4 cm of relative inflation occurred prior to mid-October 2007, then was followed by 4 cm of relative deflation. If the amount of inflation is indicative of the amount of overpressure accumulated until mid-October 2007 (an average of 0.0925 MPa) these results suggest that the deflationary event (an average of 0.07 MPa) did not fully relax the overpressure. There remains 0.02 MPa of overpressure within the SMFZ.

The rates of inflation and deflation can be simply calculated from Figure 3.4 by dividing the maximum amount of vertical deformation by the amount of time spanned by the interferograms used to make the deformation map. We find that the rate of inflation is half the rate of deflation. The inflation rate is 6.2 cm/yr assuming inflation was constant during the period of observation. The deflation rate is 15.7 cm/yr with the same assumption. This suggests that the processes for inflation are gradual whereas those responsible for deflation are more rapid.

The temporal record of the seismic events during the temporary deployment reflects the type of event related to inflation and deflation (Figure 3.11). Type 1 events are indicative of breaking rock (Cramer and McNutt, 1997), whereas Type 4 events are indicative of fluid movement (magmatic and/or meteoritic) (Figure 3.11) (Lahr et al., 1994; Cramer and McNutt, 1997). Some tremor activity could be induced by heavy rainfall. This is observed by the correlation in the amount of tremors recorded mimicking the rainfall curve (Figure 3.11). Types 2 and 3 are hybrid events with the difference being a precursor event present in Type 3. This precursory event could be indicative of fluid movement triggering the tectonic events (Lahr et

al., 1994). Type 4 activity occurs throughout the deployment. The only time Type 4 events do not account for the majority is October 2007, which is a period of overall heightened seismicity and the transition from inflation to deflation at San Miguel. Just before the transition, a few very long-period Type 4 events occurred, equivalent to a RSAM >400 units when the normal RSAM value for San Miguel is ~10-20 units (Escobar, 2007). During this time, the highest magnitude earthquakes are recorded indicating that the greatest amount of energy is also being released (Figure 3.11). Following this event, many small rockslides occurred within the summit crater. In fact, these slides were still occurring when we picked up the instruments at the end of January 2008. The spike in seismic activity is mainly Type 1 and Type 2 events, which are events that did not occur together any other time except May 2007, during another spike in seismic activity. During the heightened May 2007 period, the fumaroles in San Miguel's summit crater increased in activity (Escobar, 2007).

Based on the earthquake epicenters and event types occurring at that location, I believe that magma and (or) gases are upwelling in the northern part of the seismic zone near the summit crater where the Type 3 events occur. I believe the upwelling occurs in this location due to the large amount of Types 2, 3, and 4 events occurring in this region. I believe inflation at San Miguel volcano is due to this upwelling of gas charged magma. This happens throughout the time span prior to the climatic mid-October transition to deflation. I suggest that the deflationary process is due to the release of pressurized gas partially to the atmosphere through the fumaroles. This is associated with Types 1 and 2 events such as those seen in October 2007. There is an additional small degassing episode in May that similarly results in Types 1 and 2 events with increased fumarolic emission of gas (Escobar, 2007). I therefore suggest that a small amount of deflation, below the resolution of our InSAR results, could have occurred in May 2007.

3.5 CONCLUSIONS

Integrating the seismic and InSAR data explains geometries and processes driving the volcanism at San Miguel volcano. The surface deformation forward model using the seismic data and data from Chesner et al. (2004) yields results comparable to the observed deformation pattern found in the interferometry. Thus the surface deformation is the result of the same processes that produce the seismic activity. In addition, these processes that drive volcanism at San Miguel are localized along and within the SMFZ. Among the processes is inflation due to upwelling/intrusion of gas-charged magmas. The observed surface deformation at San Miguel is a direct result of volcanic material upwelling within the SMFZ, as shown through the surface deformation forward modeling. Another important process is deflation due to release of gas pressure, either through fumaroles and subsurface migration through fractures.

Field data and time sequence aerial photographs of the summit crater observed in Chesner et al. (2004) gives evidence that San Miguel is subsiding. This subsidence is accomplished through numerous piecemeal collapses. They describe the collapses to be associated with flank lava flows, as well. From the earthquake locations (Figure 3.8), we find that most of the scattered earthquakes west of the SMFZ occur within the southwestern slope, thus, forming a secondary fractured zone. These fractures make this slope structurally weaker, so I consider this southwestern slope to have the greatest volcano hazard when compared to the rest of the volcano's perimeter. The types of volcanic hazards we would expect are lava flows, landslides, or both. Landslides could occur if the fractured areas in the southwestern slope become lubricated with water from heavy monsoonal rains. A lava flow could occur if magma

vents out through the small fracture network. Both could occur, along with increased surface deflation, during future explosive eruptions.

3.6 ACKNOWLEDGEMENTS

I would like to acknowledge Bill Rose and Craig Chesner for their help coordinating this project in El Salvador. Galen Kaip, Todd Theiner and SNET for their help deploying the instruments. I thank the gracious people of the Cuidad de San Miguel for taking care of instruments and us. I also need to thank Stephen Hernandez for his help with the empirical seismic testing and Yuri Fialko for kindly granting me the use of his SIC program. This research was funded by NASA Earth System Science Fellowship number NNX06AF78H. ALOS data was paid for by WInSAR with NASA and NSF funds and provided by the Japan Aerospace Exploration Agency (JAXA) through the Americas ALOS Data Node (AADN) at the Alaska Satellite Facility (ASF).

3.7 REFERENCES

Agostini, S., Corti, G., Doglioni, C., Carminati, E., Innocenti, F., Tonarini, S., Manetti, P., Di Vincenzo, G., Montanari, D., 2006, Tectonic and magmatic evolution of the active volcanic front in El Salvador: insight into the Berlin and Ahuachapan geothermal areas. *Geothermics*, vol. 35, p. 368 – 408.

Ammon, C., 2008, personal communication (electronic) to Aaron Velasco (04/15/08).

BBC, 2008, http://www.bbc.co.uk/weather/world/city_guides/results.shtml?tt=TT001840, (last visited 12/0908).

Bratt, S.R., and Bache, T.C., 1988, Locating Events With a Sparse Network of Regional Arrays *Bulletin of the Seismological Society of America*, vol. 78, p. 780-798.

BRTT, 2008, http://www.brtt.com/software.html, (last visited 10/15/08).

Burgmann, R., Rosen, P.A., and Fielding, E.J., 2000, Synthetic Aperture Radar Interferometry to Measure Earth's Surface Topography and Its Deformation: *Annual Reviews of Earth and Planetary Sciences*, vol. 28, p. 169-209.

Carr, M.J., 1984, Symmetrical and segmented variation of physical and geochemical characteristics of the Central American volcanic front. *Journal of Volcanology and Geothermal Research*, vol. 20, p. 231–252.

Cramer, C.H., and McNutt S.R., 1997, Spectral analysis of earthquakes in the 1989 Mammoth Mountain Swarm near Long Valley, California. *Bulletin of the Seismological Society of America*, vol. 87, no. 6, p. 1454-1462.

Chesner, C.A., Pullinger, C., Escobar, C.D., 2004, Physical and chemical evolution of San Miguel Volcano, El Salvador. *Geological Society of America Special Paper*, vol. 375, p. 213-236.

Corti, G., Carminati, E., Mazzarini, F., Garcia, M.O., 2005, Active strike-slip faulting in El Salvador (Central America). *Geology*, vol. 33, p. 989–992.

Delacourt, C., Briole, P., and Achache, J., 1998, Troposhperic corrections of SAR interferograms with strong topography: Application to Etna. *Geophysical Research Letters*, vol. 25, no. 15, p. 2849-2852.

DeMets, C., 2001, A new estimate for present-day Cocos-Caribbean plate motion: Implications for slip along the Central American volcanic arc. *Geophysics Research Letters*, vol. 28, p. 4043-4046

Endo, E.T., and Murray, T., 1991, Real-time Seismic Amplitude Measurement (RSAM): a volcano monitoring and prediction tool. *Bulletin of Volcanology*, vol. 53, p. 533-545.

Escobar, C.D., 2007, personal communication (electronic) (10/2006 - present).

Fernandez, M., Escobar, C.D., and Redondo, C.A., 2004, Seismograph networks and seismic observation in El Salvador and Central America. *Geological Society of America Special Paper*, vol. 375, p. 257 – 167.

Fialko, Y., Khazan, Y., Simons, M., 2001a, Deformation due to a pressurized horizontal circular crack in an elastic half-space, with applications to volcano geodesy. *Geophysical Journal International*, vol. 146, p. 181–191.

Fialko, Y., Simons, M., Khazan, Y., 2001b. Finite source modeling of magmatic unrest in Socorro, New Mexico, and Long Valley California. *Geophysical Journal International*, vol. 146, p. 191– 200.

Gottsmann, J., Rymer, H., and Berrino, G., 2006, Unrest at the Campi Flegrei caldera (Italy): A critical evaluation of source parameters from geodetic data inversion. *Journal of Volcanology and Geothermal Research*, vol. 150, p. 132– 145.

Gurlap, 2008, http://www.guralp.com/, (last visited 10/15/08).

GVN Bulletin, 2002, Minor gas-and-ash emission in January 2002; Summary of earlier activity. *Bulletin of the Global Volcanology Network*, vol. 27, no. 02.

GVN Bulletin, 2006, Restlessness persists during 2005-6; heavy tropical rains trigger lahars. *Bulletin of the Global Volcanology Network*, vol. 31, no. 10.

GVN Bulletin, 2007, Background seismicity since October 2006; crater visit in July 2007. *Bulletin of the Global Volcanology Network*, vol. 32, no. 09.

IRIS, 2008, http://www.iris.edu/software/sac/, (last visited 09/20/08).

Kennett, B. L. N., and Engdahl, E. R., 1991, Travel times for global earthquake location and phase identification. *Geophysical Journal International*, vol. 105, p. 429-465.

Lahr, J.C., Chouet, B.A., Stephens, C.D., Power, J.A., 1994, Earthquake classification, location, and error analysis in a volcanic environment: implications for the magmatic system of the 1989 – 1990 eruptions at Redoubt Volcano, Alaska. *Journal of Volcanology and Geothermal Research*, vol. 62, no. 1-4, p.137– 151.

Lu, Z., Kwoun, O., and Rykhus, R., 2007, Interferometric synthetic aperture radar (InSAR): Its past, present and future. *Photogrammetric Engineering and Remote Sensing*, vol. 73, p. 217-221.

Manconi, A., Walter, T. R., and Amelung, F, 2007, Effects of mechanical layering on volcano deformation. *Geophysical Journal International*, vol. 170, no. 2, p.952-958.

Manzo, M., Ricciardi, G.P., Casu, F., Ventura, G., Zeni, G., Borgstrom , S., Berardino, P., Del Gaudio, C., Lanari, R., 2006, Surface deformation analysis in the Ischia Island (Italy) based on spaceborne radar interferometry. *Journal of Volcanology and Geothermal Research*, vol. 151, p. 399–416.

Massonnet, D., Feigl, K.L., 1998, Radar interferometry and its application to changes in the Earth's surface. *Reviews of Geophysics,* vol. 36, no. 4, p. 441-500.

Meyer-Abich, H., 1956, Los Volcanes Activos de Guatemala y El Salvador (America Central). *Anales del Servicio Geologico Nacional de El Salvador*, vol. 3, p. 49–62.

Mogi, K., 1958, Relations between the eruptions of various volcanoes and the deformations of the ground surfaces around them. *Bulletin Earthquake Research Institute*, vol. 36, p. 99-134.

Newmann, A.V., Dixon, T.H., and Gourmelen, 2006, A four-dimensional viscoelastic deformation model for Long Valley Caldera, California, between 1995 and 2000. *Journal of Volcanology and Geothermal Research,* vol. 150, p. 244 – 269.

Perez, N.M., Hernandez, P.A., Padron, E., Cartagena, R., Olmos, R., Barahoma, F., Melian, G., Salazar, P., and Lopez, D.L., 2006, Anomalous Diffuse CO2 Emission prior to the January 2002 Short-term Unrest at San Miguel Volcano, El Salvador, Central America. *Pure Applied Geophysics*, vol. 163, p. 883-896.

Rémy, D., Briole, P., Bonvalot, S., 2001, Correction of troposphereic effects in SAR interferometry data on volcanic areas: Application to Sakurajima volcano (Japan). *European Geophysical Society XXVI General Assembly*, Nice, France, March 2001.

Sandwell, D., Myer, D., Mellors, R., Shimada, M., Brooks, B., and Foster, J., 2007, Accuracy and Resolution of ALOS Interferometry: Vector Deformation Maps of the Father's Day Intrusion at Kilauea. *IEEE Transactions on Geosciences and Remote Sensing*, vol. 2007-00737.R1, p. 1-12.

Taylor, J.R., 1982, An introduction to error analysis: the study of uncertainties in physical measurements: Sausalito, Ca. University Science Books pg 60 - 76.

Velasco, A.A., Gee, V.L., Rowe, C., Grüjic, D., Hollister, L.S., Hernandez, D., Miller, K.C., Tobgay, T., Fort, M., and Harder, S., 2007, Using Small Temporary Seismic Networks for Investigation Tectonic Deformation: Brittle Deformation and Evidence for Strike-Slip Faulting in Bhutan. *Seismological Research Letters*, vol. 78, no. 4, p. 446-453.

Velasco, A.A., Hernandez, S., Parsons, T., and Pankow, K., 2008, Global ubiquity of dynamic earthquake Triggering. *Nature*, vol. 1, p.375-379.

Wadge, G., Dorta , D.O., Cole, P.D., 2006, The magma budget of Volcán Arenal, Costa Rica from 1980 to 2004. *Journal of Volcanology and Geothermal Research*, vol. 157, p. 60-74.

Waldhauser, F., and Ellsworth, W. L., 2000, A double-difference earthquake location algorithm: method and application to the Northern Hayward fault. *Bulletin of the Seismological Society of America*, vol. 90, p. 1353–1368.

Waldhauser, F., 2001, *hypoDD* -- A Program to Compute Double-Difference Hypocenter Locations *(hypoDD* version 1.0 - 03/2001). *United States Geological Survey Open File Report 01-113*, p. 25.

Yang, X.-M., Davis, P., Dietrich, J.H., 1988. Deformation from inflation of a dipping finite prolate spheroid in an elastic halfspace as a model for volcanic stressing. *Journal of Geophysical Research*, vol. 93, p. 4249– 4257.

Yun, S., Segall, P., Zebker, H., 2006, Constraints on magma chamber geometry at Sierra Negra Volcano, Galapagos Islands, based on InSAR observations. *Journal of Volcanology and Geothermal Research*, vol. 150, p. 232 – 243.

Zebker, H.A., Rosen, P.A., Goldstein, R.M., Gabriel, A., Werner, C.L., 1994, On the derivation of coseismic displacement fields using differential radar interferometry: The Landers earthquake. *Journal of Geophysical Research*, vol. 99, no. 19, p. 617-634.

Table 3.1: Image pairs used in InSAR analysis.

Start Date	End Date	$B_{\perp}$ (m)	Time Span (days)	Orbit
2/27/2007	10/15/2007	632.16	230	Ascending
2/27/2007	8/30/2007	483.39	184	Ascending
3/3/2007	10/19/2007	425.43	230	Descending
8/30/2007	10/15/2007	132.12	46	Ascending
10/15/2007	1/15/2008	127.86	92	Ascending
10/19/2007	1/19/2008	127.1	92	Descending

Table 3.2: Earthquake locations with calculated M_L.

LONG	LAT	YEAR	MONTH	DATE	HOUR	MIN	SEC	TYPE	M_L
-88.317	13.450	2007	3	29	6	32	37.2	4	-
-88.307	13.421	2007	4	9	11	11	22	4	-
-88.256	13.393	2007	4	15	5	45	9.45	4	-
-88.250	13.417	2007	5	3	3	46	45.33	1	2.21
-88.272	13.433	2007	5	7	2	55	37.6	4	-
-88.276	13.414	2007	5	11	6	1	4.06	4	-
-88.273	13.444	2007	5	11	19	18	28.44	4	-
-88.266	13.418	2007	5	21	4	0	23.8	4	-
-88.260	13.424	2007	5	23	8	41	59.67	2	2.11
-88.286	13.453	2007	5	27	18	4	50.66	4	-
-88.269	13.414	2007	7	4	7	12	44.8	4	-
-88.274	13.419	2007	7	4	9	34	39.04	4	-
-88.318	13.460	2007	7	29	7	6	30.43	4	-
-88.248	13.392	2007	7	31	10	4	53.68	4	-
-88.271	13.404	2007	8	2	1	49	37.18	4	-
-88.265	13.437	2007	8	8	4	3	40.32	4	-
-88.276	13.443	2007	8	31	8	27	35.75	3	2.44
-88.273	13.441	2007	8	31	8	47	46.48	4	-
-88.273	13.447	2007	9	3	6	25	19.59	2	2.34
-88.282	13.452	2007	9	6	7	33	57.7	3	2.53
-88.278	13.441	2007	9	8	9	35	46.91	2	2.81
-88.272	13.399	2007	9	10	22	51	51.56	4	-
-88.269	13.449	2007	9	16	17	27	57.64	2	3.56
-88.278	13.449	2007	9	18	15	6	46.04	3	3.22
-88.277	13.447	2007	9	20	3	53	36.07	3	2.81
-88.273	13.447	2007	9	21	14	22	36.59	3	2.53
-88.282	13.430	2007	9	21	23	39	3.24	4	-

-88.260	13.394	2007	9	21	23	47	33.32	4	-
-88.287	13.423	2007	9	22	2	13	52.73	4	-
-88.272	13.423	2007	9	27	3	47	32.82	4	-
-88.274	13.451	2007	9	29	3	42	57.88	4	-
-88.282	13.446	2007	10	1	20	28	1.98	1	3.29
-88.273	13.435	2007	10	3	23	9	34.12	1	2.29
-88.273	13.401	2007	10	4	15	43	49.68	4	-
-88.283	13.450	2007	10	6	7	21	44.78	4	-
-88.268	13.394	2007	10	7	1	16	27.14	2	2.81
-88.267	13.437	2007	10	7	18	56	52.5	2	3.01
-88.292	13.457	2007	10	11	6	55	41.95	2	2.92
-88.271	13.425	2007	10	12	3	27	24.67	4	-
-88.249	13.416	2007	10	13	2	0	13.94	1	2.71
-88.259	13.427	2007	10	13	7	56	25.06	1	3.22
-88.260	13.417	2007	10	13	11	23	41.43	1	2.68
-88.265	13.430	2007	10	14	23	26	15.36	1	2.61
-88.267	13.389	2007	10	15	14	20	16.9	2	3.57
-88.277	13.440	2007	10	17	6	53	52.87	1	2.35
-88.256	13.432	2007	10	18	9	21	34.62	2	2.31
-88.283	13.403	2007	10	21	9	3	36.79	2	3.06
-88.290	13.415	2007	10	21	21	59	19.2	2	3.16
-88.270	13.442	2007	10	22	10	20	3.17	2	2.32
-88.276	13.451	2007	10	23	2	52	13.87	2	2.19
-88.272	13.442	2007	10	29	15	52	53.29	1	2.76
-88.268	13.441	2007	11	8	9	57	8.89	3	2.63
-88.270	13.449	2007	11	12	4	34	12.12	2	2.88
-88.308	13.447	2007	11	26	17	43	59.92	4	-
-88.256	13.444	2007	12	2	7	45	45.05	2	2.38
-88.293	13.437	2007	12	6	5	44	29.37	4	-

-88.308	13.457	2007	12	24	23	55	10.92	2	3.14

3.3: List of parameters used in surface deformation forward model.

Variable			Value	Unit
Satellite Azimuth	Ascending Orbit		-11	Degrees
	Descending Orbit		-169	Degrees
Look Angle	Ascending Orbit		33.8	Degrees
	Descending Orbit		35	Degrees
Satellite Wavelength			23.3	cm
Standard Deviation for Noise			0	mm
Shear Modulus (μ)			5	GPa
Poisson's Ratio			0.25	
Depth to source center (d)			600	m
Yang	Semi-major axis of ellipsoid		500	m
	Semi-minor axis of ellipsoid		166	m
	Strike (Azimuth) of semi-major axis of ellipsoid		168	Degrees (from north)
	Dip of semi-major axis of ellipsoid		89.5	Degrees (from horizontal)
Mogi	Diameter of Circular Mogi Source		500	m
Fialko	Ratio of depth/radius		1.2	
Maximum Excess Magma Pressure Calculation		Density of Solid Rock (ρ)	2800	kg/m^3
		Minimum Chamber Radius (a_{min})	450	m
		Volume Change (ΔV)	2.5	m^3
		Maximum Excess Magma Pressure (Δp_{max})	42	MPa

Excess Magma Pressure	Yang	Inflation	Ascending Orbit	0.065	MPa
			Descending Orbit	0.12	MPa
		Deflation	Ascending Orbit	-0.09	MPa
			Descending Orbit	-0.05	MPa
	Mogi	Inflation	Ascending Orbit	0.006	MPa
			Descending Orbit	0.0095	MPa
		Deflation	Ascending Orbit	-0.0075	MPa
			Descending Orbit	-0.0045	MPa
	Fialko	Inflation	Ascending Orbit	0.006	MPa
			Descending Orbit	0.0105	MPa
		Deflation	Ascending Orbit	-0.0075	MPa
			Descending Orbit	-0.0045	MPa

Table 3.4: Root Mean Square (RMS) error between interferogram and corresponding model.

Interferogram	Yang (cm)	Mogi (cm)	Fialko (cm)
02/27/2007 - 10/15/2007	0.42	0.55	0.51
03/03/2007 - 10/19/2007	1.15	1.16	1.18
10/15/2007 - 01/15/2008	0.75	0.78	0.87
10/19/2007 - 01/19/2008	2.31	2.34	2.42

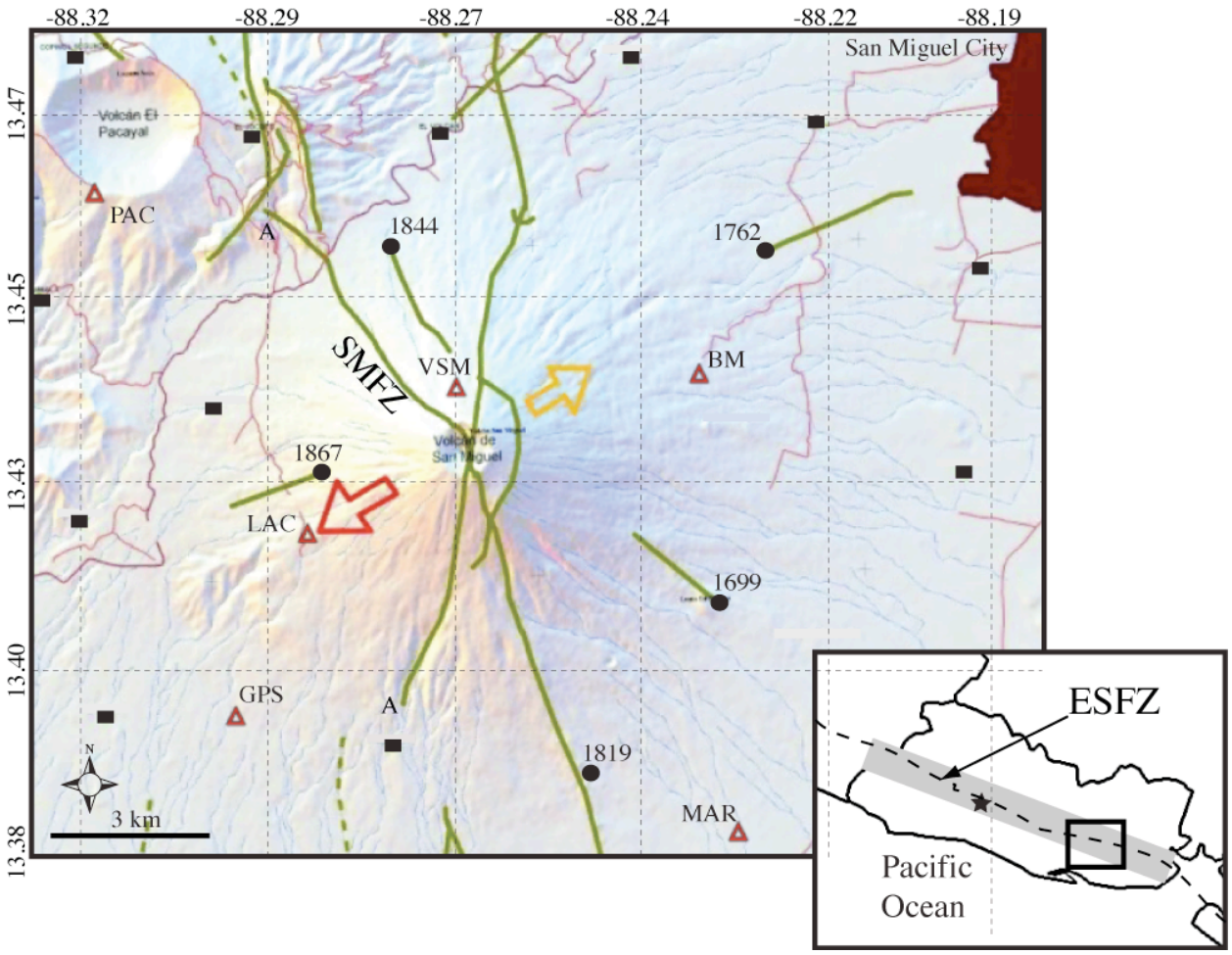

Figure 3.1: Map of San Miguel volcano (Escobar, 2007). Inset shows location of study area in El Salvador. Black dashed line in inset indicates location of El Salvador Fault Zone (ESFZ). Gray shaded area around black dashed line is the Median Trough. Green lines are fractures mapped by SNET. The fracture marked A is the San Miguel Fracture Zone (SMFZ). Triangles denote seismometers. Circles are locations of the vents that fed historic lava flows within the year of eruption. Squares are small villages. Black polygon in upper right is the city of San Miguel. Red lines are highways. Red and yellow arrows represent the tensile stress direction for the SMFZ.

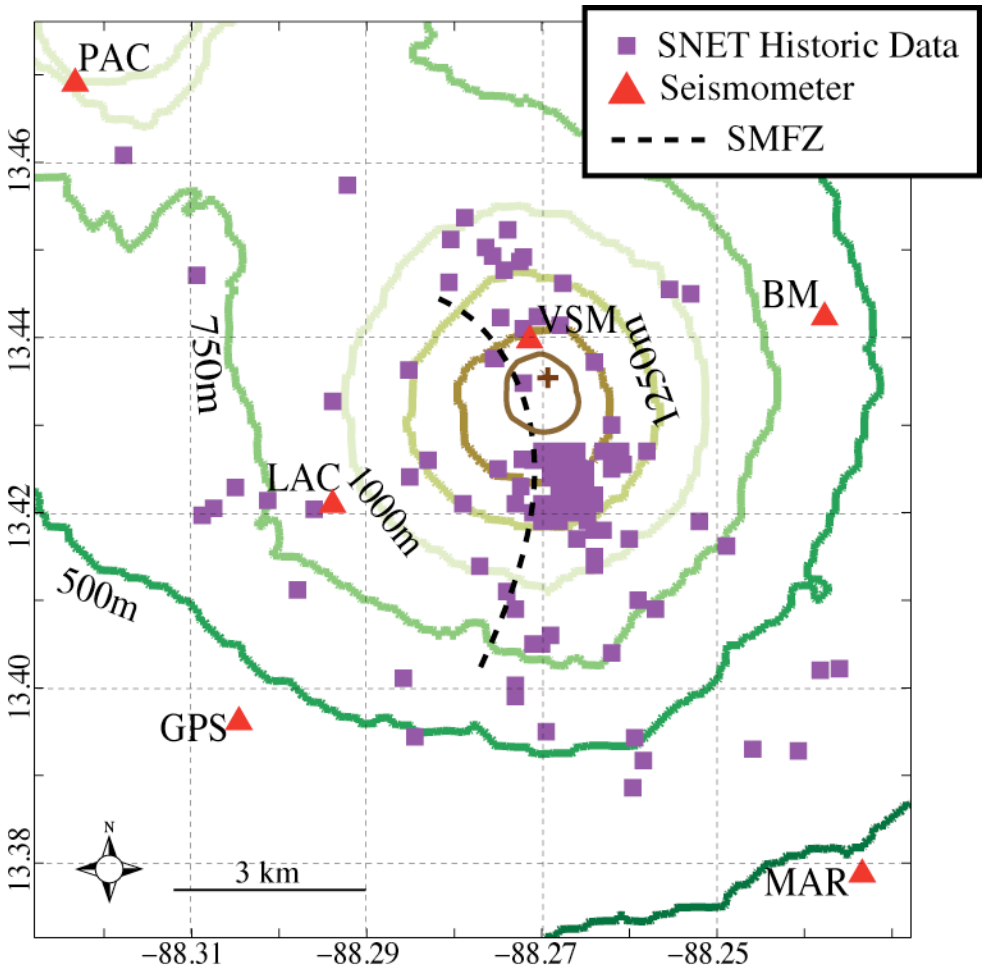

Figure 3.2: Historic seismicity (1984 – 2007) map (Escobar, 2007). Triangles denote the locations of seismometers in the temporary seismic network. Historic seismicity has been recorded by SNET seismometers at PAC, LAC, VSM, and BM. The historic seismicity has a local magnitude (M_L) range of 1.5 – 5. Green through brown contours indicates elevation. Cross is San Miguel volcano summit.

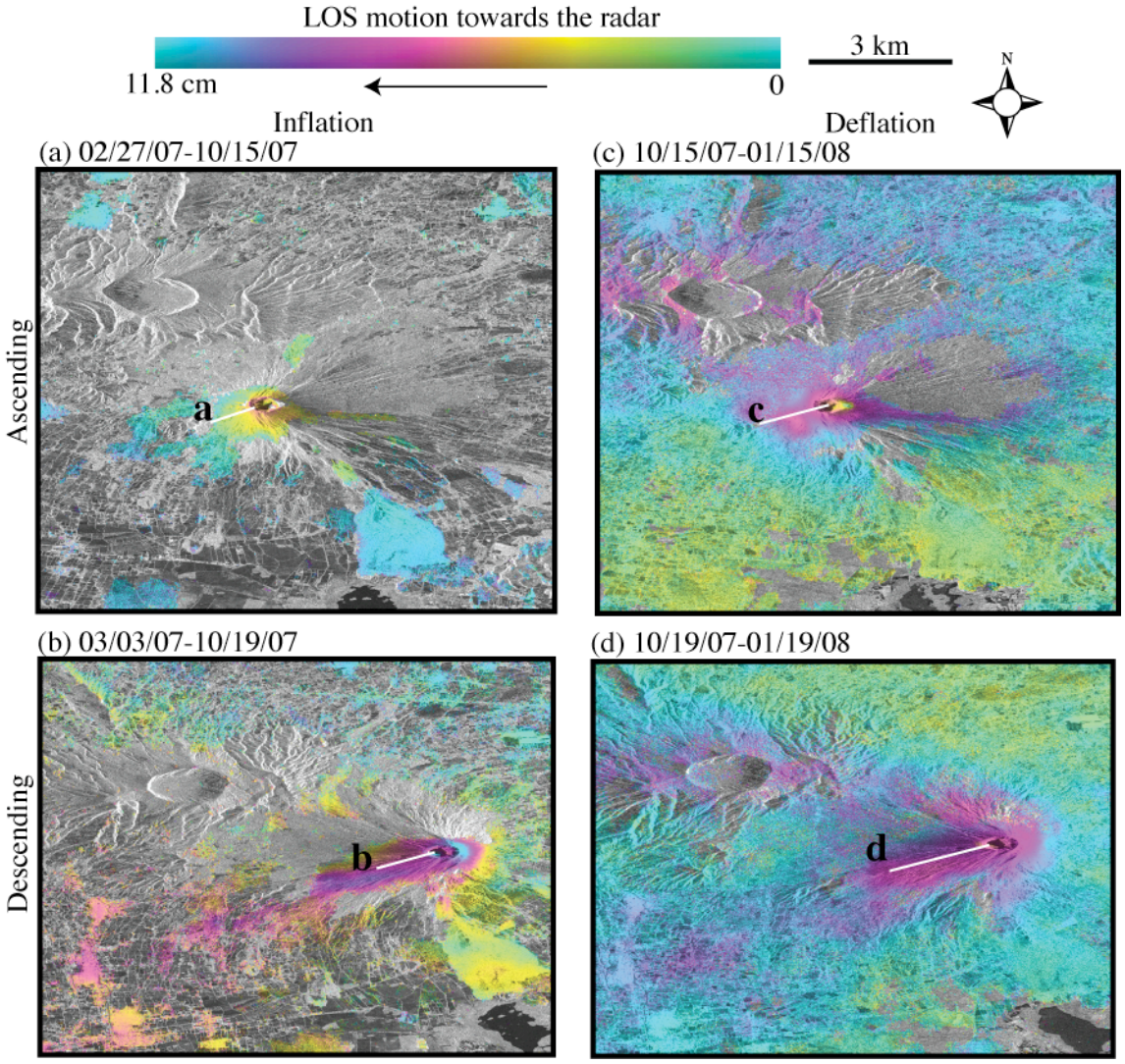

Figure 3.3: Interferograms of San Miguel volcano: (a) 02/27/07-10/15/07, (b) 03/03/07-10/19/07, (c) 10/15/07-01/15/08, and (d) 10/19/07-01/19/08. Interferograms (a) and (c) are obtained from ascending orbits. Interferograms (b) and (d) are obtained from descending orbits. Interferograms, (a) and (c), prior to mid-October 2007 show inflation. The interferograms, (b) and (d), after mid-October 2007 show deflation, and have negative motion (e.g. away from the satellite). White lines indicate profiles in Figure 3.4. Gray areas are decorrelated regions in the interferogram.

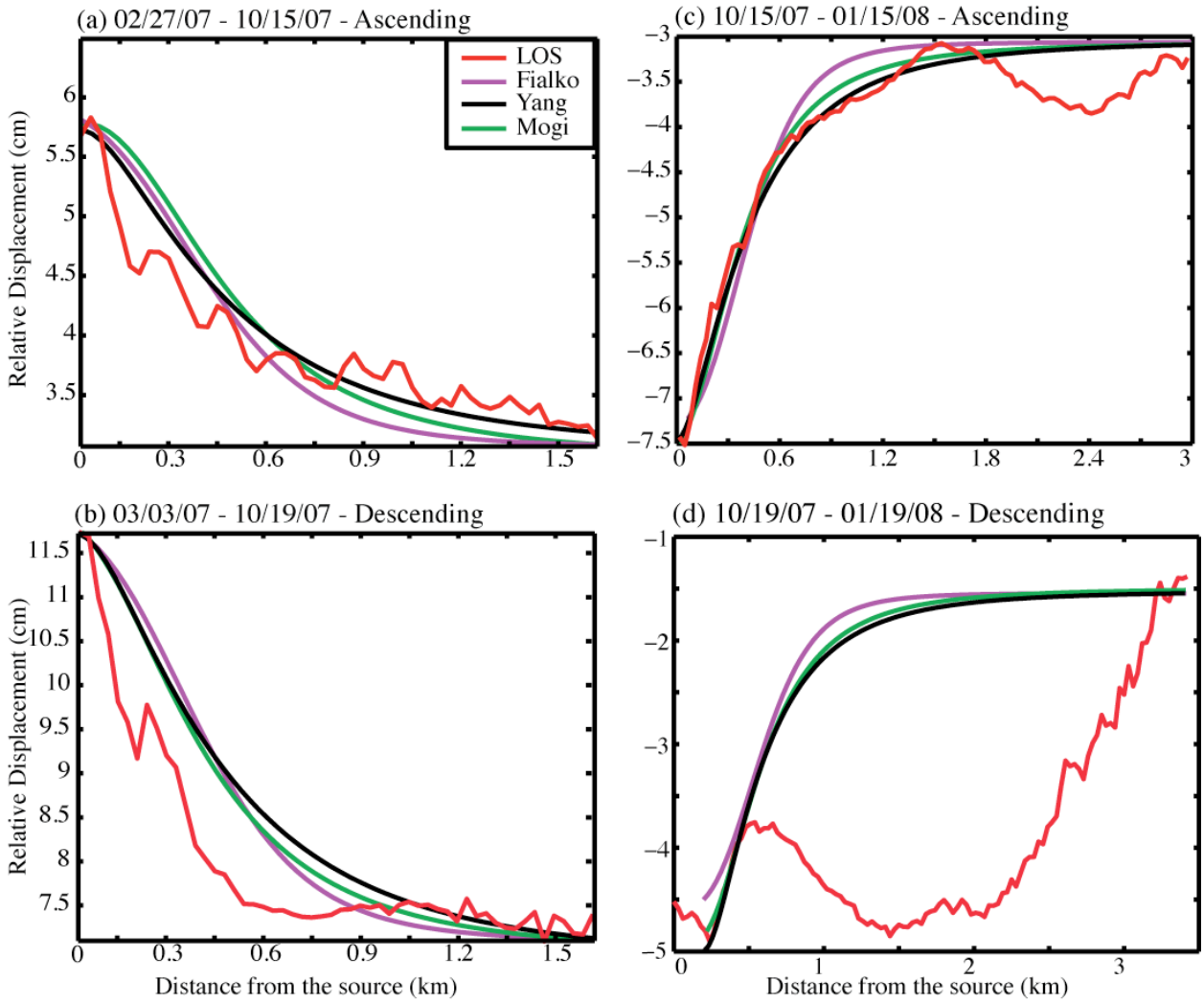

Figure 3.4: Deformation profiles from the interferograms in Figures 3.3. Positive red profiles show inflation, and are taken from Figures 3.3(a-b). Negative red profiles show deflation, and are taken from Figures 3.3(c-d). Black, green, and purple are forward model profiles.

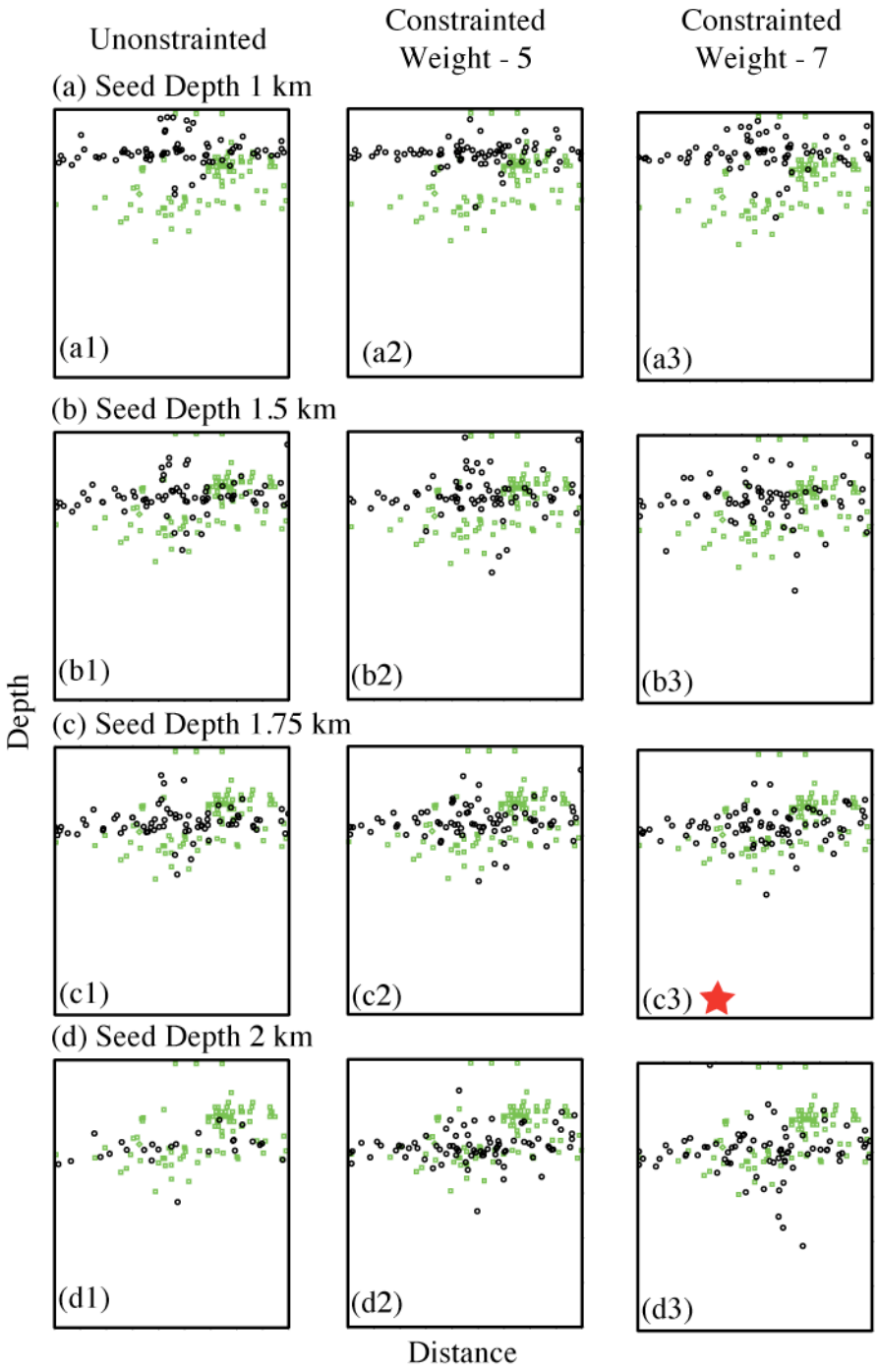

Figure 3.5: Hypocenter sensitivity test. Each cross-section is 9 km wide and 6 km deep. Sections are taken along profile line D-D' in Figure 3.8. Columns are model runs with same constraint and weight. Rows are model runs with same seed depth. Black circles are calculated locations using the given parameters. Green squares are historic seismicity from SNET (1986-2007) (Escobar, 2007). Red star denotes the preferred locations and cross-section used in the surface deformation forward model.

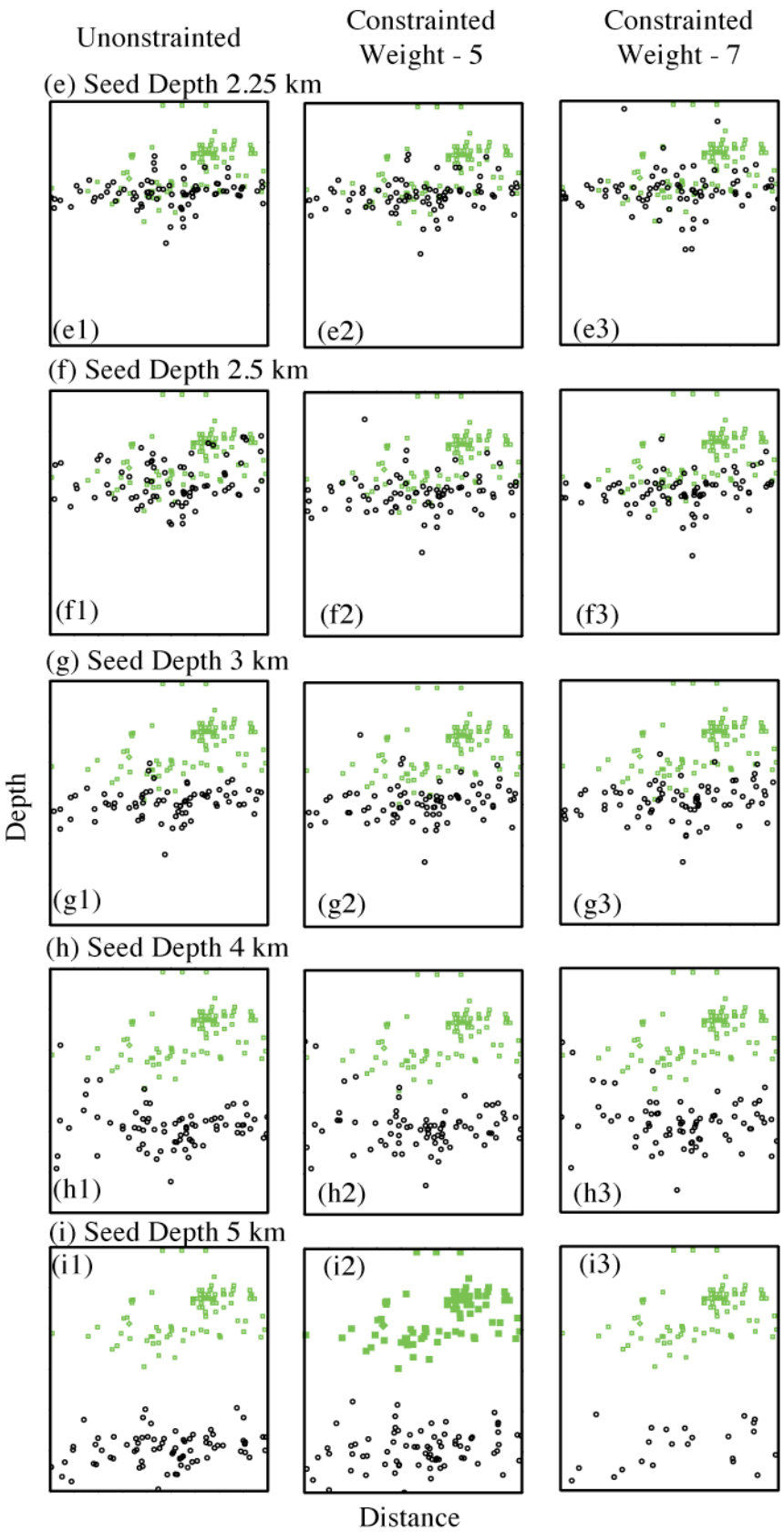

Figure 3.5 continued.

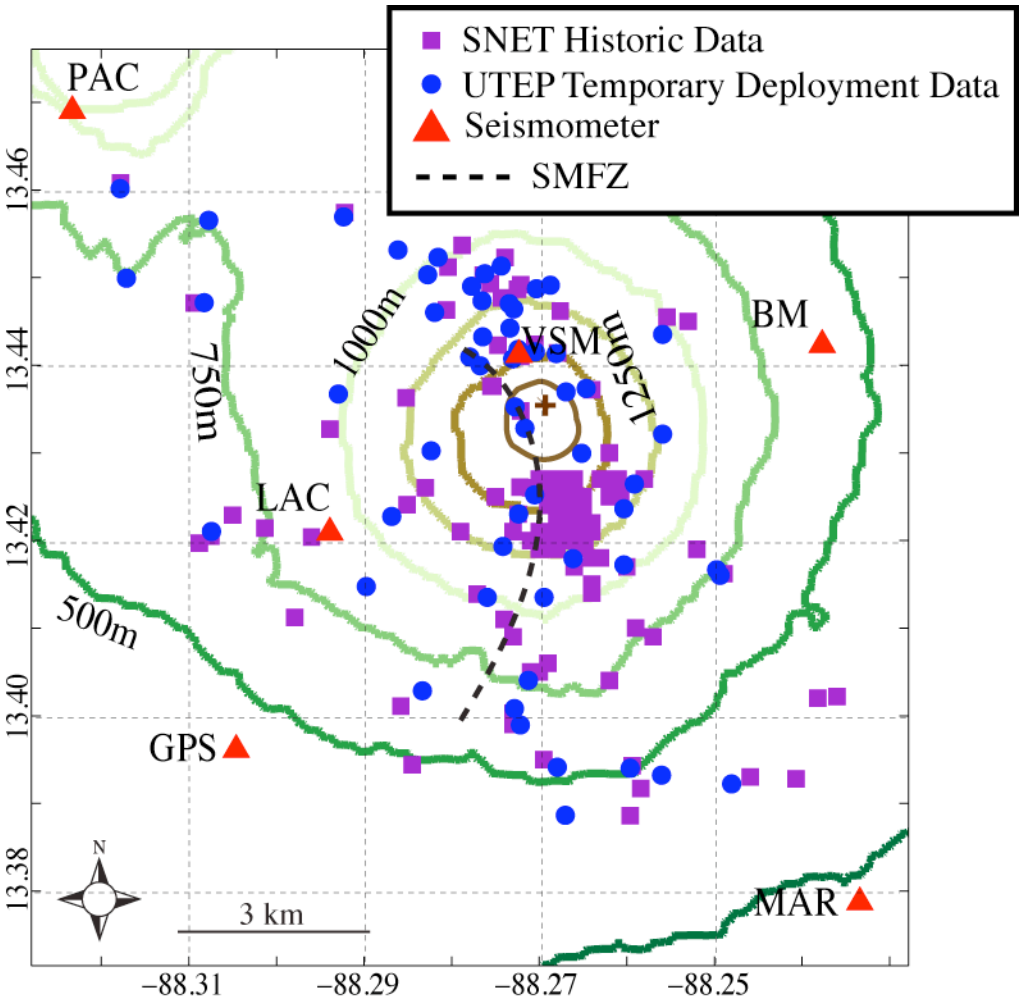

Figure 3.6: Epicentral locations from the temporary seismic deployment (March 2007 – January 2008) with historic activity (1984 – 2007) (Escobar, 2007).

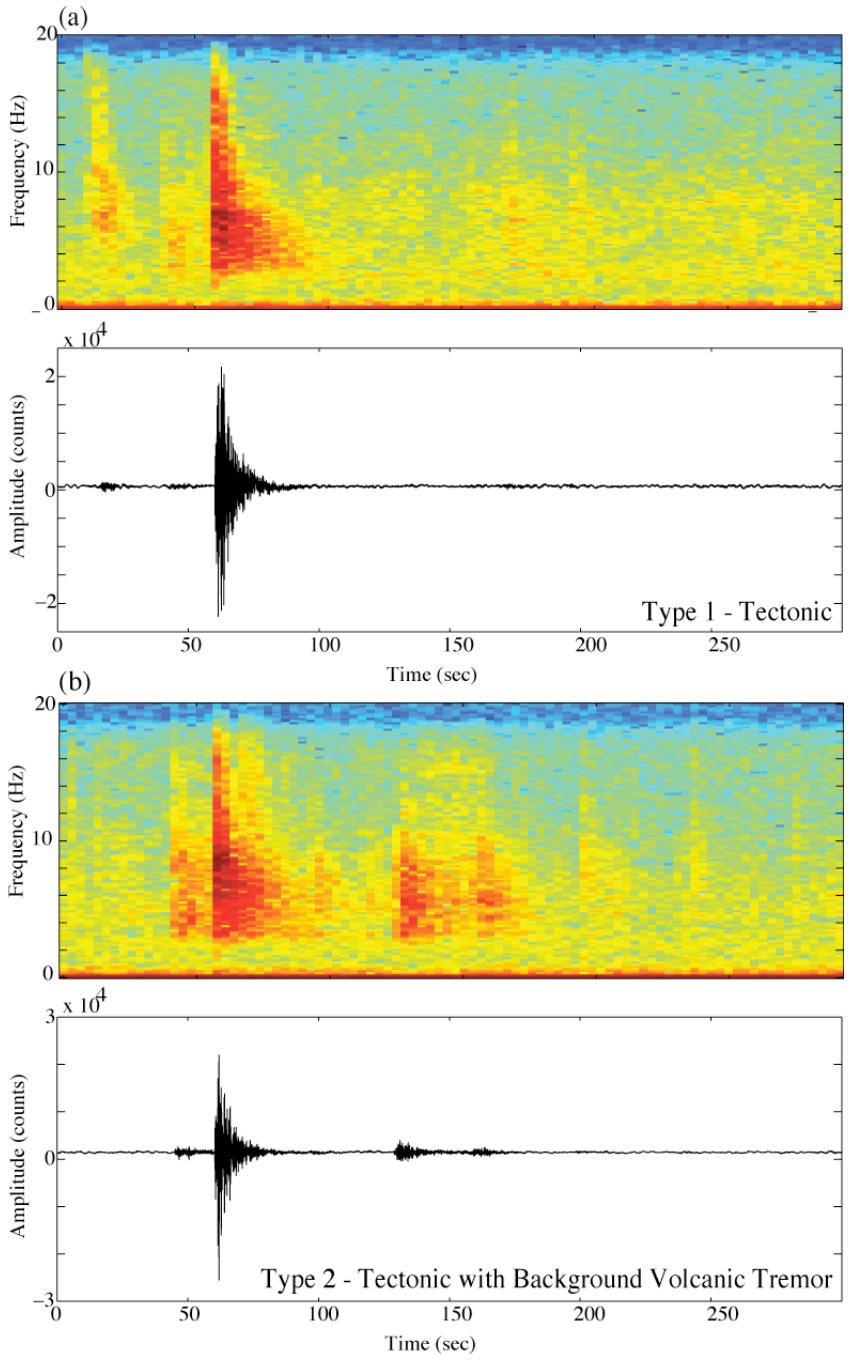

Figure 3.7: Example seismic events with different source types from our classification: (a) Tectonic; (b) Tectonic with Volcanic Tremor; (c) Tectonic with a Precursory Event and Volcanic Tremor; (d) Volcanic Tremor. Top panel of each set is the calculated spectrogram. Each spectrogram depicts the frequencies captured at a specific time in the waveform. Bottom panel of each set is the seismogram used to calculate the spectrogram. Seismograms are from the VSM station.

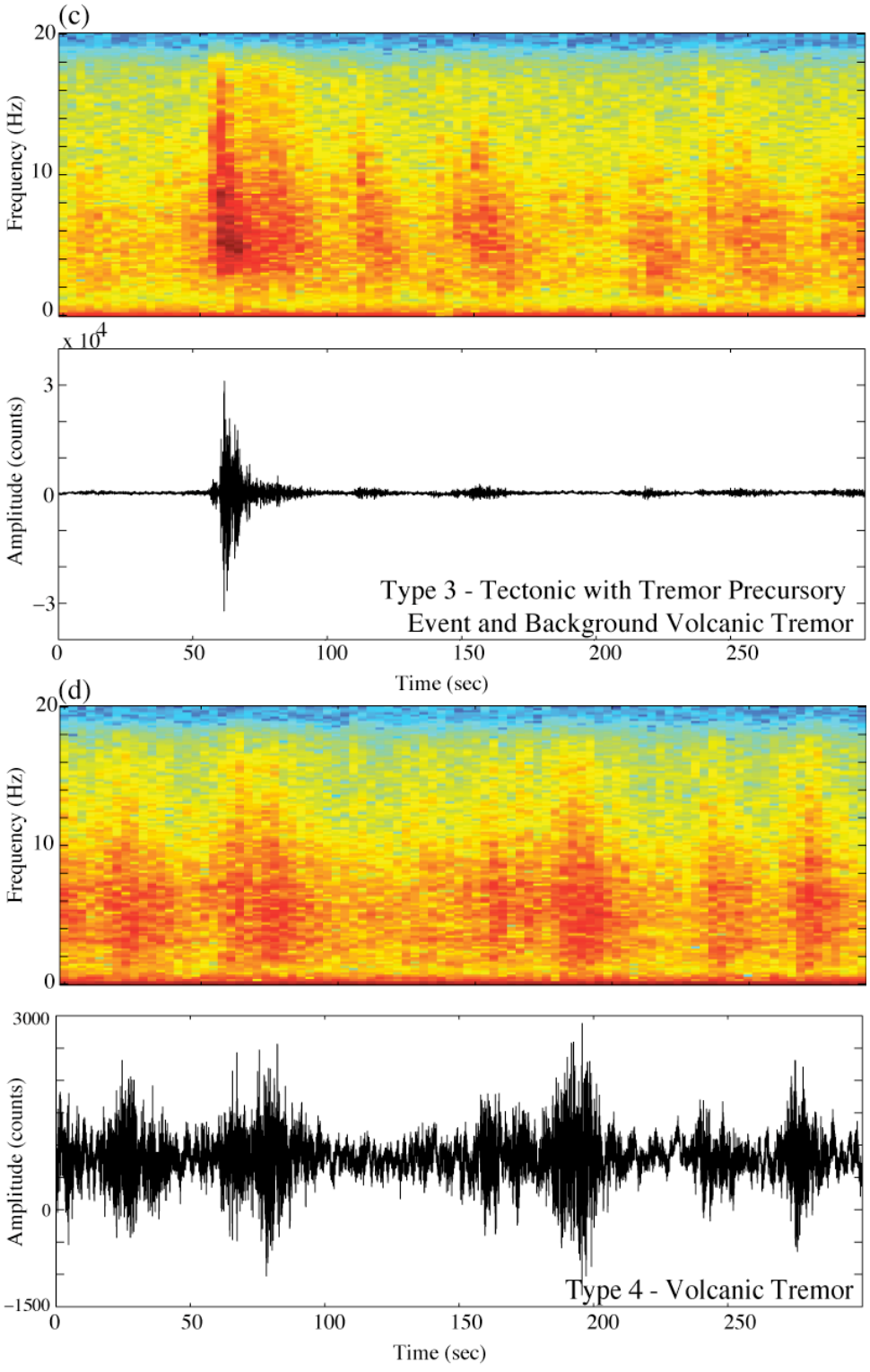

Figure 3.7 continued.

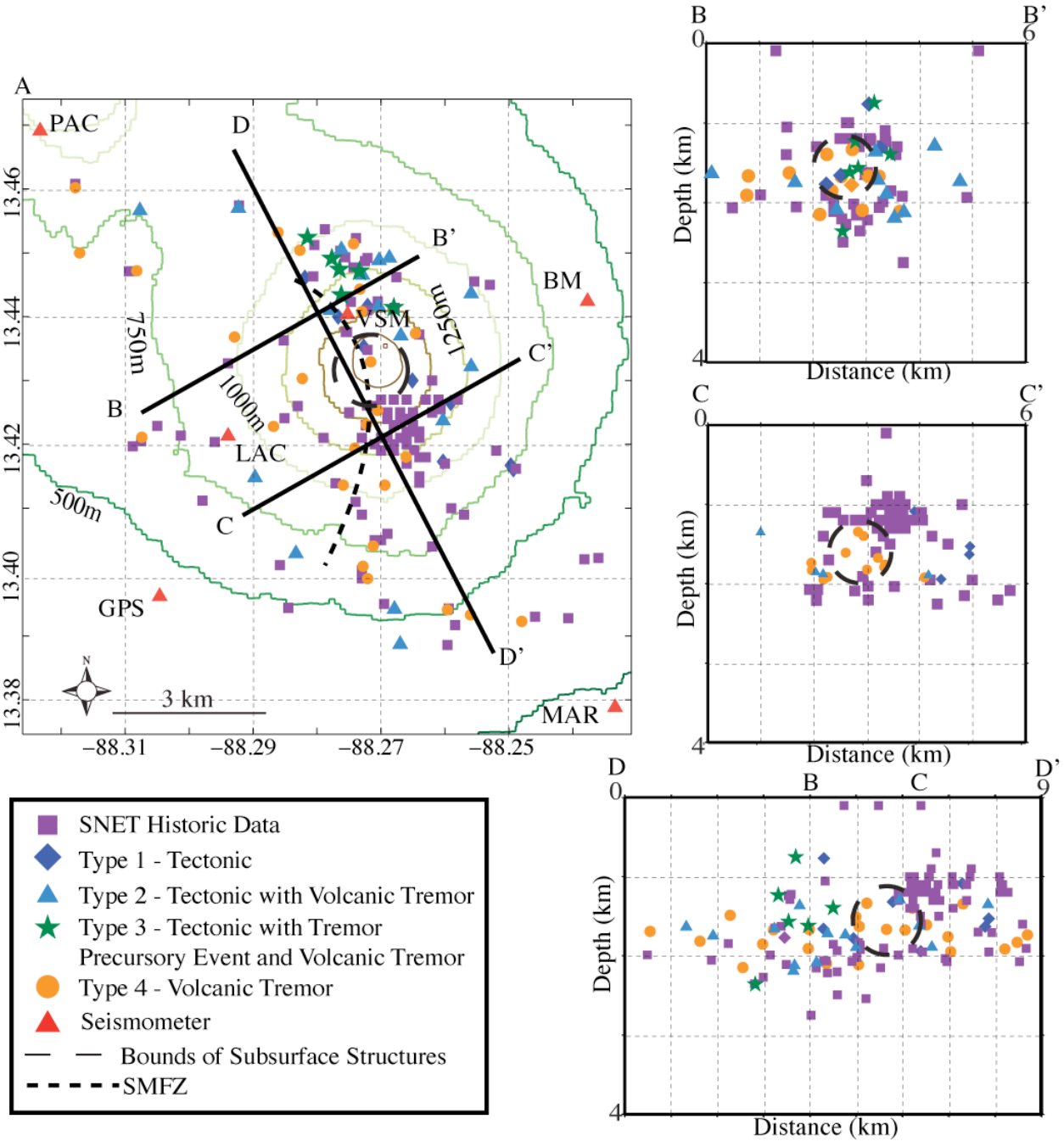

Figure 3.8: Hypocentral locations of events with different source types. (a) Classified earthquake locations using the results of the temporary seismic network and SNET (Escobar, 2007) historic data. (b) Cross-section at northern end. (c) Cross-section at southern end. (d) Cross-section along strike of the SMFZ. Cross-sections (b) and (c) include events 2 km from the profile line.

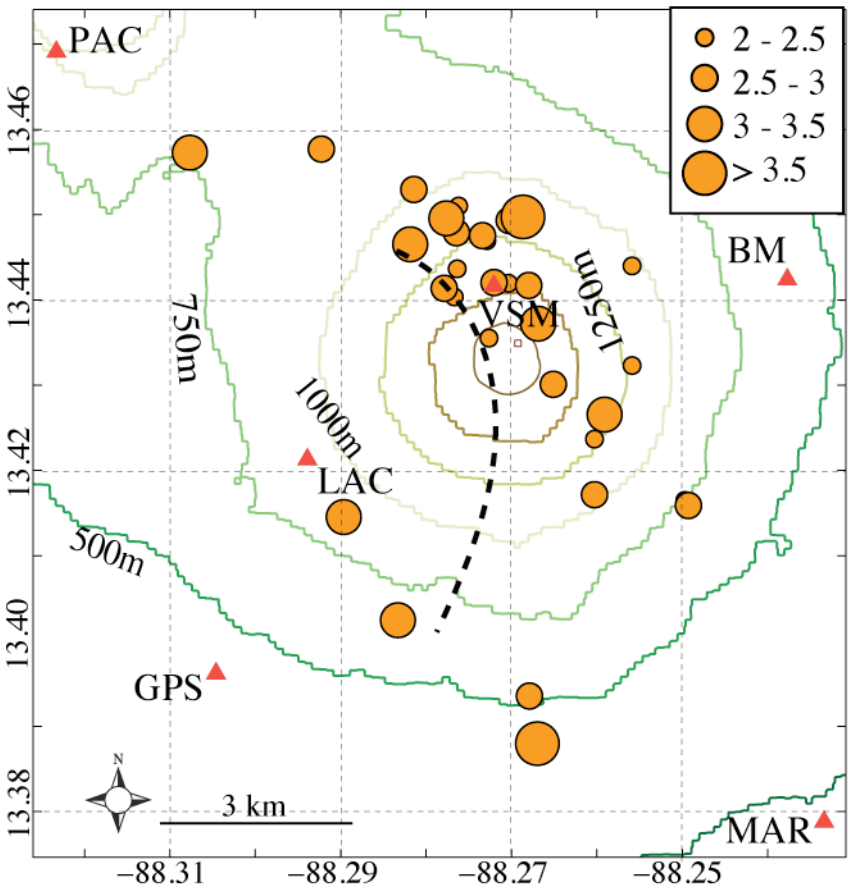

Figure 3.9: Epicentral earthquake locations listed in Table 3.2 scaled to local magnitude (M_L). These magnitudes represent classified earthquakes of types 1-3.

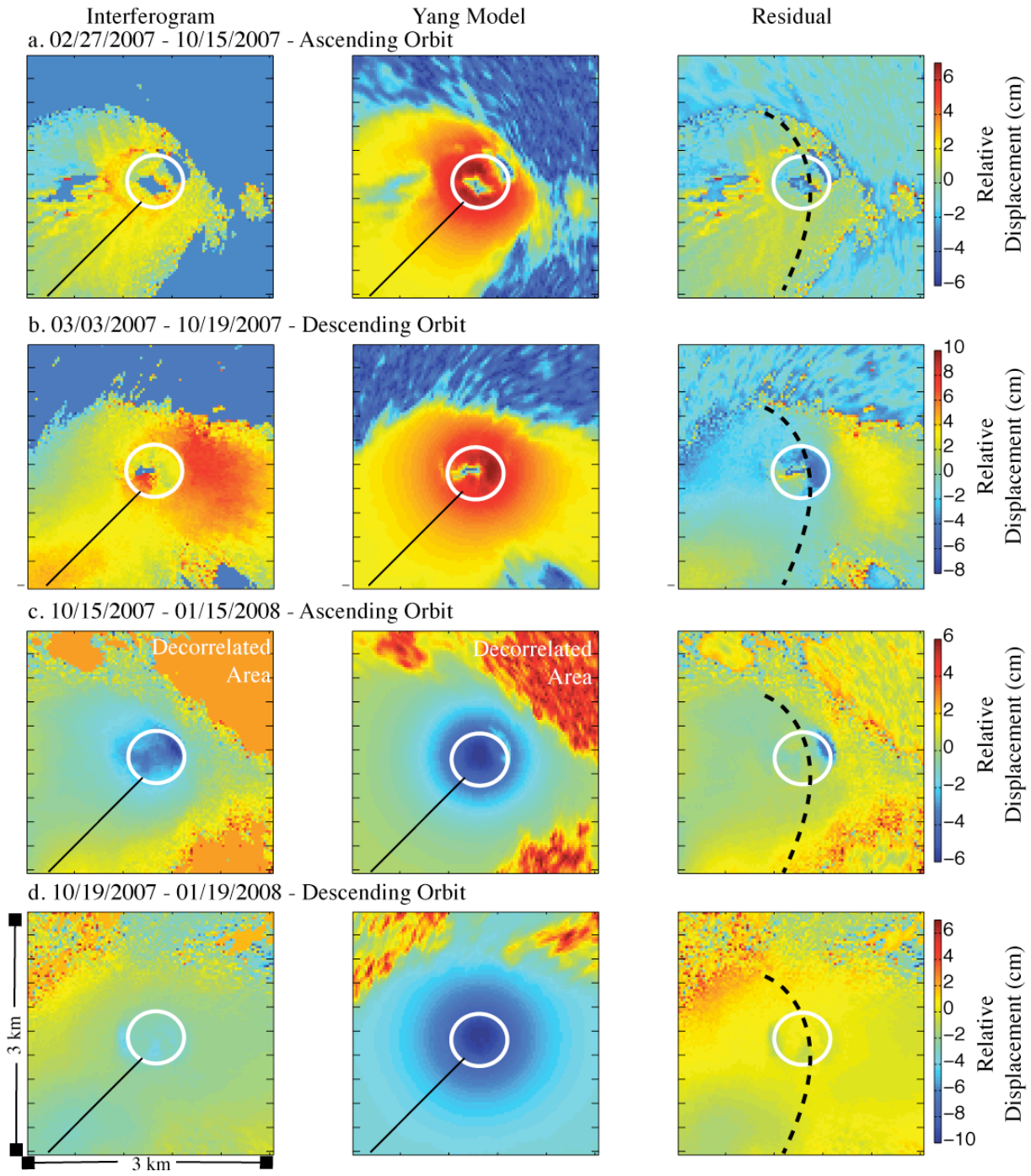

Figure 3.10: Results from Yang forward model. LOS displacement map (left column) with corresponding synthetic LOS interferograms (middle column), and residual map (right column). Yang source parameter models are based on seismic analysis results and work by Chesner et al. (2004). White circle is the outline of summit crater at San Miguel. Black line indicates profile shown in Figure 3.4. Color scale given at the end of row corresponds to that row. Black dashed line is the placement of the SMFZ. Models include noise addition from corresponding interferogram correlation map.

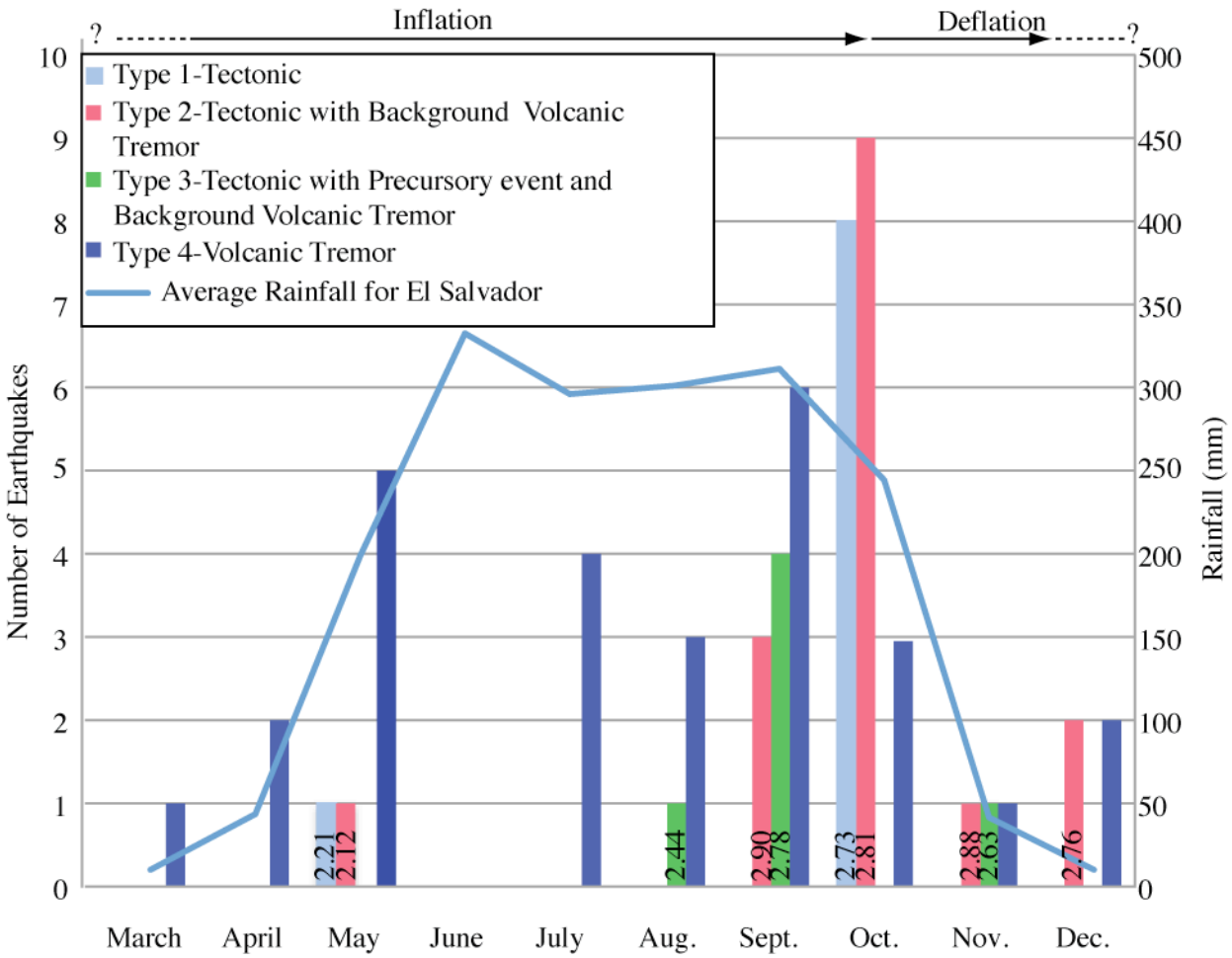

Figure 3.11: Temporal distribution of the classified earthquakes (not including historic events) shown in Figure 3.8. Numbers in bars are average M_L results for that event type during that month. Line represents average rainfall of El Salvador from BBC (2008).

CHAPTER 4

SYNTHESIS

The goal of this dissertation is to characterize surface and subsurface deformation patterns of reservoir systems. The interaction between the surface deformation patterns and geophysically derived subsurface structures is explored through modeling, and enables an understanding of how these complex, dynamic systems work. This goal was achieved in two different projects. Each project had the following common objectives:

- To utilize InSAR for detecting and quantifying surface deformation;
- To integrate surface deformation data with geophysical measurements to build structural and deformation models of the reservoir;
- To determine the relationships between measured surface deformation fields and subsurface structures.

In the course of my two projects, I successfully met these objectives, and gained interesting insights.

In Chapter 2, "Determining the Influences of Anthropogenic Land Subsidence in the Mimbres Basin Near Deming, NM using InSAR, Gravity, and Storage Coefficient Calculations," I established that the Mimbres Basin has undergone a maximum of 9.2 cm of subsidence over the 5 yr period. The subsidence is heterogeneous, wherein the western portion of the Basin is experiencing 11 mm/yr of subsidence and outside of this area the basin is subsiding at a rate of 17 mm/yr. The mechanism driving the fast compaction rate may be the dehydration of a thick deposit of lacustrine clays or sub-terra subterranean cavity filling.

In Chapter 3, "Determining Volcanic Deformation at San Miguel Volcano, El Salvador by Integrating Radar Interferometry and Seismic Analyses," I show that the surface deformation

is driven by the upwelling of gas-charged magma along a fracture zone running through the summit crater of San Miguel. However, the southwestern slope of the volcano has the worst structural integrity and has the highest potential for volcanic hazards such as landsliding.

Together these projects demonstrate the dynamics of reservoir systems. First, these projects demonstrate that surface deformation is directly linked to a subsurface process. Second, these systems are complex, and while aspects of their behavior may be understood using simple models, their complete description requires an integrative approach. For example, complexities in composition, geometry, structural integrity, and influx (e.g. pumping or intrusion) of material into and out of the system are all important parameters to quantify in modeling. These issues are encountered in the Mimbres Basin results, where a portion of the basin is deforming faster than the rest of the basin. The integrative approach was essential at San Miguel in order for the surface deformation modeling to be done. Third, these systems react to changes in their environments in short (e.g., earthquakes) and long (e.g. seismic tremor) time scales. Fourth, these projects also show that integrating geophysical data and models with deformation profiles from InSAR aids in determining how faults manifest themselves within deformation fields. An example of this is observed in Deming, NM.

In all, the processes I was able to capture through these studies lead me to suggest strategies for further monitoring in each of the study areas. Further monitoring of these systems will entail additional radar interferometry, Light Detection and Ranging (LIDAR) analysis, and further seismic monitoring. For the Deming, NM chapter (Chapter 2), monitoring of these sites can be continued with time-series radar interferometry analyses. These analyses will aid in determining if the water conservation methods (e.g. desalination, decline in evaporative cooling methods, etc.) adopted by the municipalities in these areas have decreased and possibly reversed

the subsidence in this Basin. This area's monitoring can also include using LIDAR to intensively map earth fissures, and a seismic geophysical survey to determine if the fast compaction rate is caused by subterranean cavity filling. The further monitoring of all of these sites will aid in determining the following questions: (1) how does subsidence patterns change over two decades? (2) How do water-preserving techniques impact future grounds subsidence patterns? (3) What causes heterogeneous deformation to occur at different well sites within the same aquifer?

For the San Miguel volcano project, I plan to continue collaboration with my colleagues at UTEP, SNET, and UT-Austin to monitor the area with more InSAR and to perform a seismic tomography analysis. The tomography analysis will aid in determining where hot spots (magma) are located in the volcano. This will help determine whether volcanic tremor seismic events are caused by magmatic or gas accumulation. This will also better constrain the geometry of the subsurface magma chamber(s) and improve further deformation modeling. I also intend to do more seismic processing with the collected seismic data to determine higher precision earthquake locations using cross-correlation analyses (e.g., Rowe et al., 2004; DeSchon et al., 2007). In addition, with receiver functions, it will be possible to better constrain crustal thickness and overall crustal structure at San Miguel (Ammon, 1991). I also plan to expand collaborative work in El Salvador, by analyzing the tectonic relationship between the El Salvador Fault Zone and the location of Quaternary volcanoes.

4.1 REFERENCES

Ammon, C. J., 1991, The isolation of receiver effects from teleseismic P waveforms. *Bulletin of the Seismological Society of America*, vol. 81, p. 2504-2510.

DeSchon, H.R., C.H. Thurber and C.A. Rowe, 2007, High-precision earthquake location and three-dimensional P-wave velocity determination at Redoubt volcano, Alaska. *Journal of Geophysical Research*, vol. 112, no. B07312, doi:10.1029/2006JB004751.

Rowe, C.A., C. H. Thurber and R. A. White, 2004, Dome growth behavior at Soufriere Hills Volcano, Montserrat, revealed by relocation of volcanic event swarms, 1995-1996. *Journal of Volanology and Geothermal Research*, vol. 134, p. 199-221.

APPENDIX A:
TUTORIAL FOR SEISMIC PROCESSING

1. Transfer field collected seismic data from binary format to RefTeK format. This is done using Passcal's Neo program. This program can be downloaded from http://www.passcal.nmt.edu/software/software.html. Figure 1 below shows a screen shot of the program. To use, simply type neo in your terminal window. Next the Neo screen will open. Put the directory your raw data is located in the 'Source' box, and put the directory where you want the processed data in the 'Destination' box. Make sure you have RefTek selected. Select convert, and this should be done in about 5 min. You can check the progress of the transfer by clicking on log in the Neo interface. When you are finished transferring data, click on done, and the interface will close. Do not run multiple sets at once.

   The most common errors are due to not having the correct computer environment set-up. Add these lines to your environment set-up:

   - setenv LD_LIBRARY_PATH /usr/local/lib:/usr/local/src/passcal/tcl8/Solaris/lib,
   - setenv PYTHON /usr/local/src/passcal/bin,
   - setenv TCL_LIBRARY /usr/local/src/passcal/tcl8/Solaris/lib/tcl8.4, and
   - setenv PASSCAL /usr/local/src/passcal.

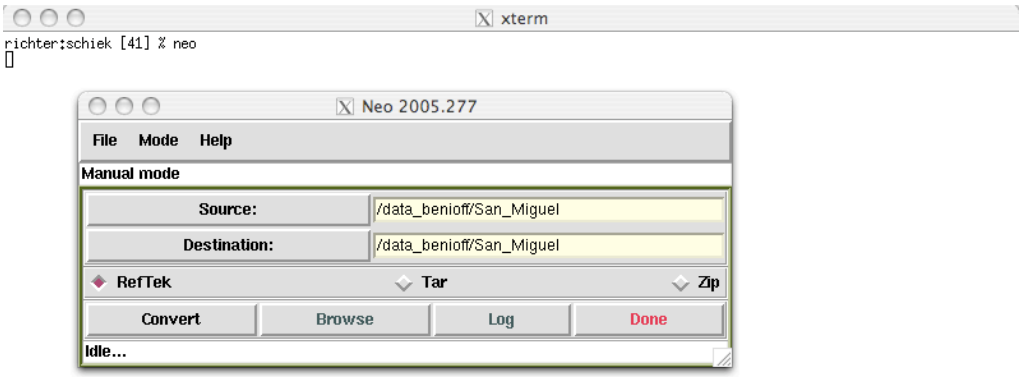

Figure 1: Snapshot of Passcal's Neo interface.

2. The *filename*.ref file is then translated to miniseed hour volumes and logs by using these Passcal commands.

   setenv LD_LIBRARY_PATH /usr/ucblib

   ref2mseed -f *filename*.ref PVFX

   ref2log -f *filename*.ref

3. This step involves putting the data in an Antelope database. The hourly miniseed volumes now need to be further processed using a sequence of commands developed by Mary Templeton in 2004. This workflow can be obtained from Aaron Velasco. The result of this workflow is an Antelope database with day miniseed volumes. These day miniseed volumes will be in a directory named after the year the data was collected in. At this point, the hourly miniseed volumes, the ones that start with R*JULIAN_DAY_NUMBER*, can be deleted. Deletion is only advised for completed seismic deployments, and on-going deployments.

4. The data are now ready for processing, picking, association for hypocenters, and tomography. The following Antelope 4.8 commands are useful for determining hypocenters and continued processing using EvLoc and HypoDD. Example *filename*.pf

files needed for commands can be obtained from Aaron Velasco. Values listed in the *filename*.pf are empirically found values that are unique to the San Miguel volcano dataset. Further descriptions for these commands can be found at http://www.brtt.com/software.html.

dbdetect	To run a detection for first arrivals using STA/LTA windowing parameters giving in dbdetect.pf.
dbgrassoc	spatial grid search based associator/locator using parameters in dbgrassoc.pf
ttgrid	creates spatial grid to be used dbgrassoc from parameters in ttgrid.pf

Cara Schiek, Cleat Zeiler, Aaron Velasco, and Stephen Hernandez designed this tutorial.

APPENDIX B:
INPUT FILES FOR HYPODD

1. PH2DT.INP

```
* ph2dt.inp - input control file for program ph2dt
* Input station file:
stations.dat
* Input phase file:
phase.dat
*MINWGHT: min. pick weight allowed [0]
*MAXDIST: max. distance in km between event pair and stations [200]
*MAXSEP: max. hypocentral separation in km [10]
*MAXNGH: max. number of neighbors per event [10]
*MINLNK: min. number of links required to define a neighbor [8]
*MINOBS: min. number of links per pair saved [8]
*MAXOBS: max. number of links per pair saved [20]
*MINWGHT MAXDIST MAXSEP MAXNGH MINLNK MINOBS MAXOBS
  0.001   25    5     20     4      4      10000
```

2. HYPODD.INP

```
*hypodd.inp:
*   INPUT FILE SELECTION
* filename of cross-cor diff. time input:
dt.cc
* filename of catalog travel time input:
dt.ct
```

```
* filename of initial hypocenter input:
event.dat
*filename of station input:
stations.dat
*
*   OUTPUT FILE SELECTION
* filename of initial hypocenter output:
SM_hypoDD.loc
* filename of relocated hypocenter output:
SM_hypoDD.reloc
* filename of station residual output:
SM_hypoDD.sta
* filename of data residual output:
SM_hypoDD.res
* filename of takeoff angle outpu:
SM_hypoDD.scr
*
*   DATA SELECTION
*IDAT:  0 = synthetics; 1= cross corr; 2= catalog; 3= cross & cat
* IPHA: 1= P; 2= S; 3= P&S
* DIST:max dist [km] between cluster centroid and station
* IDAT    IPHA    DIST
   2       1     500
*
*   EVENT CLUSTERING:
* OBSCC:    min # of obs/pair for crosstime data (0= no clustering)
* OBSCT:    min # of obs/pair for network data (0= no clustering)
```

```
* OBSCC   OBSCT
   0       4
*
*   SOLUTION CONTROL:
* ISTART:       1 = from single source; 2 = from network sources
* ISOLV:        1 = SVD, 2=lsqr
* NSET:         number of sets of iteration with specifications following
*  ISTART  ISOLV  NSET
  2       1      2
*
*   DATA WEIGHTING AND REWEIGHTING:
* NITER:              last iteration to use the following weights
* WTCCP, WTCCS:       weight cross P, S
* WTCTP, WTCTS:       weight catalog P, S
* WRCC, WRCT:         residual threshold in sec for cross, catalog data
* WDCC, WDCT:         max dist [km] between cross, catalog linked pairs
*       ---  CROSS DATA -----        ----CATALOG DATA ----
* NITER   WTCCP  WTCCS  WRCC  WDCC  WTCTP   WTCTS  WRCT  WDCT  DAMP
  8     -9     -9   -9   -9    1    -9     -9     -9    190
  8     -9     -9   -9   -9    1    -9      6      2    175
*
*--- 1D model:
* NLAY:         number of model layers
* RATIO:        vp/vs ratio
* TOP:          depths of top of layer (km)
* VEL:          layer velocities (km/s)
* NLAY  RATIO
```

12   1.73

*MAM-LONG VALLEY CALDERA model from HypoDD example 3 . Depth to top, velocity

* TOP

0.0 0.5 1.0 2.0 3.0 5.0 7.0 10.0 14.0 18.0 30.0 50.0

* VEL

3.55 3.57 3.70 5.35 5.67 5.90 6.02 6.07 6.10 6.18 6.67 8.00

*--- event selection:

* CID: cluster to be relocated (0 = all)

* ID: ids of event to be relocated (8 per line)

* CID

 0

* ID

CURRICULUM VITAE

Cara Schiek is originally from Joliet, IL. She attended Eastern Illinois University in Charleston, IL receiving a Bachelors of Science in Geology in 2002. Her undergraduate research was mainly in the area of igneous petrology and optical mineralogy under the direction of Dr. Craig Chesner, and she completed a senior thesis titled: *A Geochemical Study of the Escuintla and La Democracia Debris Avalanches, Guatemala*. Additionally, she published two abstracts with Dr. Chesner at AGU and GSA. In her spare time, she worked as an intern in numerous departments at the Illinois State Geological Society.

In the fall of 2002 she entered the graduate program in Geological Sciences at University of Texas at El Paso and developed a new interest in neotectonics and geophysics. After finishing her Masters in Geology under the guidance of Dr. José Hurtado in 2004, she continued with her graduate work with Dr. José Hurtado and Dr. Aaron Velasco. After completing her Ph.D., she will be taking an employment opportunity as a Geoscience Researcher at Royal Dutch Shell.

Permanent e-mail address: cara78@earthlink.net

This dissertation was typed by Cara G. Schiek.